



# Low-pressure isobaric cooling metamorphic $P$ – $T$ paths from Botnnuten in the southern Lützow-Holm Complex, East Antarctica

Sotaro Baba<sup>1</sup> · Seira Ohshiro<sup>1</sup> · Atsushi Kamei<sup>2</sup> · Tomokazu Hokada<sup>3,4</sup> · Ipppei Kitano<sup>5,6</sup>

Received: 16 February 2023 / Accepted: 22 April 2024 / Published online: 19 June 2024  
© The Author(s), under exclusive licence to Springer-Verlag GmbH Austria, part of Springer Nature 2024

## Abstract

This paper reports the metamorphic texture of cordierite megacrysts and the metamorphic  $P$ – $T$  path of a newly exposed section of gneiss in East Antarctica. We used mineral textures and pseudosection modeling to reconstruct the metamorphic  $P$ – $T$  path of cordierite- and spinel–garnet-bearing gneisses from Botnnuten, an isolated nunatak located ~60 km from the southern edge of Lützow-Holm Bay in East Antarctica. The gneisses underwent low- $P$  granulite-facies metamorphism at 5.0–6.1 kbar and  $850 \pm 20$  °C followed by isobaric cooling. The isobaric cooling path implies long residence in the middle to shallow crustal level without rapid exhumation. This contrasts with the widely recognized clockwise  $P$ – $T$  path of basement rocks of the Lützow-Holm Complex. The rocks at Botnnuten have long been considered part of the Lützow-Holm Complex based on their petrographical features and geothermobarometric data. However, the present results, combined with a reevaluation of available data, indicate the metamorphic history of the Botnnuten gneisses is more comparable to that of the Yamato Mountains, located southwest of the study area.

**Keywords** East Antarctica · Lützow-Holm Complex · Metamorphic  $P$ – $T$  path · Isobaric cooling

## Introduction

The evaluation of metamorphic  $P$ – $T$  paths is critical for reconstructing tectono-thermal events and the tectonic setting of metamorphic rocks. During exhumation, the  $P$ – $T$  path of high-grade metamorphic rocks typically shows isothermal decompression (ITD) or isobaric cooling (IBC). It has been hypothesized that the former is

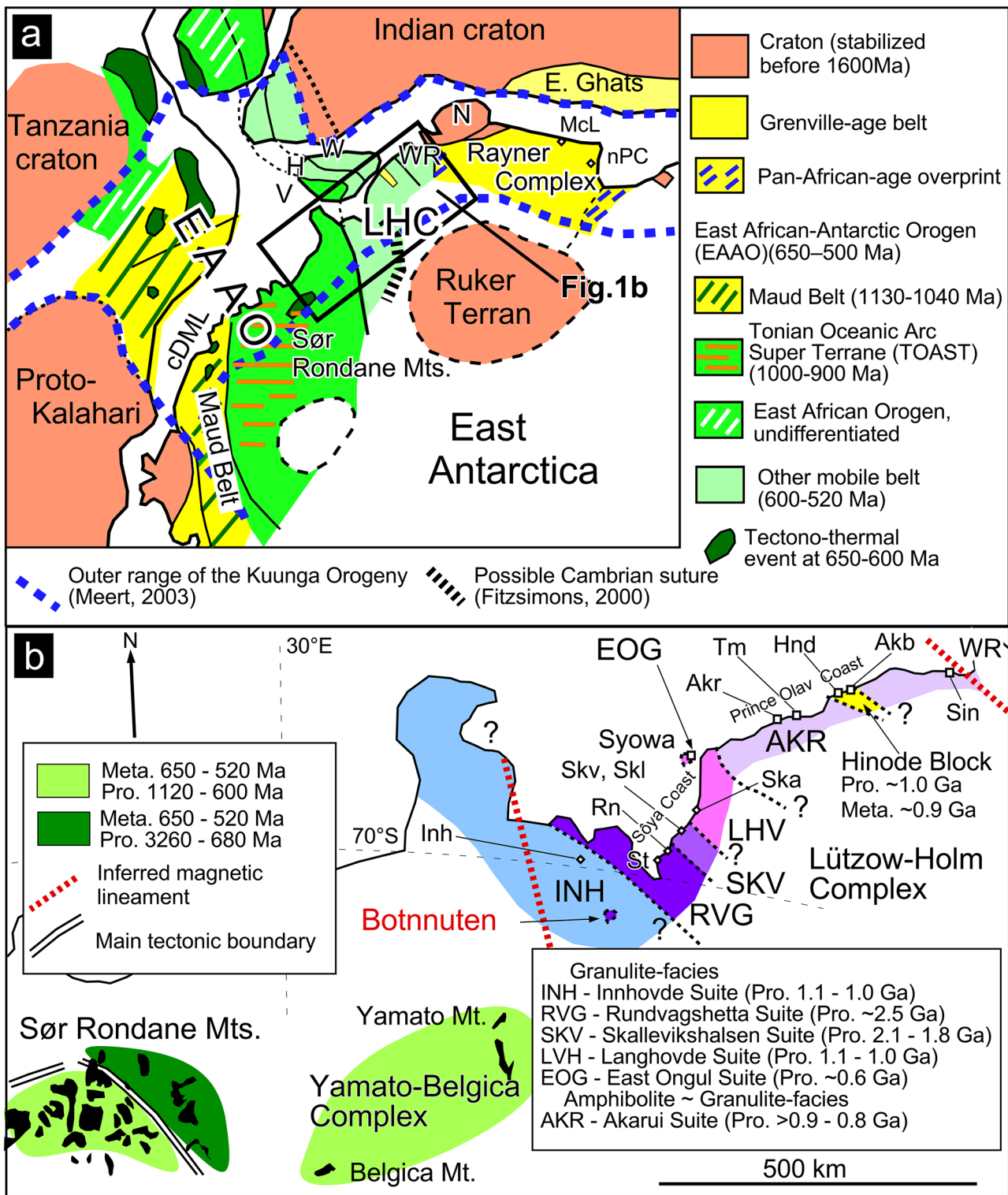
due to the rapid erosion or uplift of metamorphic rocks in response to extensional tectonics after continental collision, and that the latter is due to magmatic loading in an extensional setting (e.g., Bohlen 1987, 1991; Harley 1989; Brown 1993). In many cases, IBC has been shown to occur during the retrograde stage of counter-clockwise  $P$ – $T$  paths (Harley 1989; Bohlen 1991), but hybrid  $P$ – $T$  paths showing early ITD and late IBC have also been reported (e.g., White et al. 2002; Baba et al. 2019). In general, many metamorphic terranes show evidence of ITD, which is considered to reflect the rapid exhumation of lower crustal rocks due to orogenic collapse or isostatic rebound of over-thickened crust formed by collisional orogeny (England and Thompson 1984; Thompson and England 1984; Harley 1989; Brown 1993).

The Lützow-Holm Complex (LHC) in East Antarctica is an Ediacaran–Cambrian orogenic belt that yields U–Pb zircon ages of 600–520 Ma (Shiraishi et al. 1994, 1997). The LHC was located in the center of the Gondwana supercontinent, which was formed by the global scale orogenesis involved convergent tectonics, which is termed as the East Africa–Antarctica Orogen (EAAO; Fig. 1a; Jacobs and Thomas 2004) at 650–500 Ma, or two separate East Africa Orogen (EAO) events (Stern 1994) at  $650 \pm 50$  Ma and the

Editorial handling: A. Möller

✉ Sotaro Baba  
baba@edu.u-ryukyu.ac.jp

- <sup>1</sup> Department of Science Education, University of the Ryukyus, Okinawa 903-0213, Japan
- <sup>2</sup> Department of Earth Science, Shimane University, Matsue, Shimane 690-8504, Japan
- <sup>3</sup> National Institute of Polar Research, Tokyo 190-8518, Japan
- <sup>4</sup> Polar Science Program, Graduate Institute for Advanced Studies, SOKENDAI, Tokyo 190-8518, Japan
- <sup>5</sup> Division of Earth Sciences, Faculty of Social and Cultural Studies, Kyushu University, Fukuoka 819-0395, Japan
- <sup>6</sup> The Hokkaido University Museum, Hokkaido 060-0810, Japan



subsequent Kuunga Orogeny at  $550 \pm 50$  Ma (Meert 2003). The LHC records a clockwise metamorphic  $P$ - $T$  path involving ITD (Yoshimura et al. 2008), as is evidenced by textures related to the breakdown of garnet to form orthopyroxene

and plagioclase symplectites (e.g., Santoshi and Yoshida 1992; Takahashi and Tsunogae 2017; Takamura et al. 2020). The LHC is typically described as a collisional belt that was active during 600–500 Ma and extends through Sri Lanka,

**Fig. 1** **a** Reconstruction of East Antarctica and adjacent parts of Gondwana at 500 Ma (after Fitzsimons 2000; Shiraishi et al. 2008; Jacobs et al. 2015; Ruppel et al. 2018). The Lützow-Holm Complex (LHC) is situated adjacent to the East African–Antarctic Orogen (EAAO). Key sutures and orogenic belts are taken from Fitzsimons (2000) and Meert (2003). Abbreviations: H=Highland Complex, N=Napier Complex, V=Vijayan Complex, W=Wanni Complex, WR=Western Rayner Complex, cDML=central Dronning Maud Land, McL=MacRobertson Land, nPC=northern Prince Charles Mountains. **b** Overview map of LHC, Yamato Belgica Complex and Sør Rondane mountains. Divisions of the LHC based on the protolith ages is after Dunkley et al. (2020). Main tectonic boundary in the Sør Rondane Mountains is taken from and Osanai et al. (2013). Abbreviations: Rn=Rundvågshetta, Skv=Skallevikshalsen, Skl=Skallen, Ska=Skarvsnes, Inh=Inhovde, Akr=Akarui Point, Hnd=Cape Hinode, Tm=Tenmondai Rock, Akb=Akebono Rock, Sin=Sinnan Rock, Meta.=age of metamorphism, Pro.=age of protolith

South India, and Madagascar (e.g., Shiraishi et al. 1994, 2008; Meert 2003; Boger et al. 2015; Osanai et al. 2016; Durgalakshmi et al. 2021). Detailed metamorphic studies of the LHC have been conducted at several exposures along the Sôya Coast (Fig. 1b; e.g., Rundvågshetta: Kawasaki et al. 2011, Hiroi et al. 2019; Skallevikshalsen: Kawakami et al. 2016), revealing peak  $P$ – $T$  conditions of 13–15 kbar and ~ 1040 °C, and that ITD cooling was involved with the interaction of a Cl-rich fluid (Kawakami et al. 2016) and the supercooling of melt inclusions (Hiroi et al. 2019). The LHC plays a crucial role in expanding our knowledge of a global geological structure beyond the orogenic belt. Moreover, it enhances our understanding of metamorphic processes and geofluids in the middle to lower crust.

Previous studies revealed that the metamorphic grade of the LHC shows a progressive increase from amphibolite to granulite-facies toward the southwest from Sinnan Rocks to Rundvågshetta (Fig. 1b; e.g., Hiroi et al. 1991; Yoshimura et al. 2008). Regional metamorphism of the entire LHC was considered to occur from Ediacaran to Cambrian (c. 600–520 Ma) (Shiraishi et al. 1994, 2008). These observations are inconsistent with recent reports of a local ultrahigh-temperature (UHT) thermal event of ~ 11–12 kbar and ~ 900–920 °C at Akarui Point (Fig. 1b) (Iwamura et al. 2013) and  $P$ – $T$  conditions of ~ 11 kbar and ~ 830–850 °C estimated by Zr-in-rutile geothermometry and kyanite/sillimanite stability at Akarui Point, Skarvsnes, and Skallen (Suzuki and Kawakami 2019). Moreover, exposures of amphibolite-facies rocks at Akebono Rock in the eastern part of the LHC yield older (Tonian) metamorphic ages (Baba et al. 2021, 2022; Kitano et al. 2023) and kyanite-bearing pelitic gneisses preserve evidence for a counter-clockwise  $P$ – $T$  path at Tenmondai Rock (Fig. 1b) (Baba et al. 2023), suggesting further investigation of the LHC is needed.

As outlined above, the metamorphic history of the entire LHC is complex and poorly understood due to isolated

exposures surrounded by glaciers. During a survey of the 58th Japanese Antarctica Research Expedition, we visited the isolated inland nunatak of Botnnuten, located 60 km from the southern edge of Lützow-Holm Bay. We found coarse-grained cordierite-bearing gneisses containing large cordierite grains up to 18 mm in diameter, which had not been reported previously in the LHC. Although the  $P$ – $T$  path of the LHC is characterized by ITD, the diagnostic ITD breakdown texture of garnet to form cordierite has been reported only in limited exposures that contain high-Mg lithologies (e.g., at UHT Rundvågshetta: Motoyoshi and Ishikawa 1997; Yoshimura et al. 2008; Hiroi et al. 2019), and cordierite itself is rare in the granulite-facies zone of the LHC. In this study, we report the petrography and model the metamorphic  $P$ – $T$  paths of both cordierite- and spinel–garnet-bearing gneisses with the aim of reconstructing the regional tectono-thermal events in the LHC. The  $P$ – $T$  paths show IBC trajectories that differ from those reported in previous works.

## Geological setting

### Lützow-Holm Complex

The LHC, an Ediacaran to Cambrian orogenic belt, occupies a vast area of about 500 km between the Western Rayner Complex (WRC) and the Yamato Mountains in East Antarctica (Fig. 1a and b; Shiraishi et al. 1994; 1997). Many studies have referred to the LHC as a 600–500 Ma continental collisional belt that also extends through Sri Lanka, South India, and Madagascar (e.g., Shiraishi et al. 1994, 2008; Meert 2003; Boger et al. 2015; Osanai et al. 2016).

The LHC consists of amphibolite- to granulite-facies metamorphic rocks and post-metamorphic intrusive rocks (Fig. 1b). The metamorphic rocks comprise quartzofeldspathic, intermediate to mafic, pelitic to psammitic gneisses, charnockites, granitoids, and calcareous and ultramafic rocks. The LHC is characterized by: 1) a progressive increase in metamorphic grade towards the southwest from Sinnan Rocks to Rundvågshetta (Fig. 1b; Hiroi et al. 1991); 2) a clockwise metamorphic  $P$ – $T$  path inferred from kyanite relics within garnet porphyroblasts, which is considered to apply to the entire LHC (Hiroi et al. 1991; Yoshimura et al. 2008); 3) metamorphic ages of 600–520 Ma, obtained by sensitive high-resolution ion microprobe (SHRIMP) and laser ablation–inductively coupled plasma–mass spectrometry (LA-ICP-MS) zircon dating (Shiraishi et al. 1994, 1997; Dunkley et al. 2014, 2020; Takahashi et al. 2018; Takamura et al. 2018); and 4), which are inferred to date the timing of UHT metamorphism at Rundvågshetta (Fig. 1b), in the southwestern part of the region (Motoyoshi and Ishikawa

1997; Yoshimura et al. 2008; Kawasaki et al. 2011). As stated earlier, the latest data contradict the previous understanding of progressive metamorphism and timing in the LHC, indicating the need for revision.

Recently, the LHC has been subdivided into; 1) three tectonic units comprising a ca. 2.5 Ga continental crust, a ca. 1.0 Ga magmatic arc and a Neoproterozoic suture zone base on geochemical and geochronological data (e.g., Tsunogae et al. 2014; 2015; Takamura et al. 2018, 2020), or 2) six geological provinces known as the Innhovde Suite, Rundvågshetta Suite, Skallevikshalsen Suite, Langhovde Suite, East Ongul Suite, and Akarui Suite (Fig. 1b) based on protolith age and lithological characterization (Dunkley et al. 2020).

## Botnnuten

Botnnuten (70°24'S, 38°01'E) is an isolated nunatak located ~170 km SSW of Syowa Station in East Antarctica. It comprises well-layered felsic and mafic gneisses, with subordinate calc-silicate rock, orthopyroxene-bearing orthogneiss (charnockite), and pelitic gneiss. The entire metamorphic sequence is ~400 m thick, and the foliation dips at  $\leq 10^\circ$  to the E or NE. The rocks in the middle-upper parts of the sequence are slightly more felsic than those in the lower part. Motoyoshi and Shiraishi (1985) reported metamorphic phase relations and geothermobarometry data that indicate the Botnnuten rocks reached  $P$ - $T$  conditions of 5–6 kbar and 750–800 °C, and they concluded that the Botnnuten gneisses represent low-pressure rocks of the LHC. Dunkley et al. (2020) reported that charnockite and garnet-bearing semi-pelitic gneisses from Botnnuten yield protolith ages of  $2472 \pm 20$  Ma and metamorphic ages of 590–550 Ma, respectively, and they interpreted the Botnnuten rocks as a klippe belonging to the Rundvågshetta Suite. During field investigations, we observed that a cliff on the northeastern side of the nunatak had collapsed, exposing a fresh surface (Fig. 2a). Samples of cordierite-bearing gneiss (SB17011802A, hereafter BTN02A) and spinel–garnet-bearing gneiss (SB17011802F, hereafter BTN02F) were collected from large, angular blocks (up to 10 m in length) located directly beneath the exposed cliff face. These samples are representative of the upper lithologies of the Botnnuten metamorphic sequence.

## Analytical methods

### Mineral composition

Prior to electron probe micro-analysis (EPMA), polished sections were covered with ~20 nm of electrically

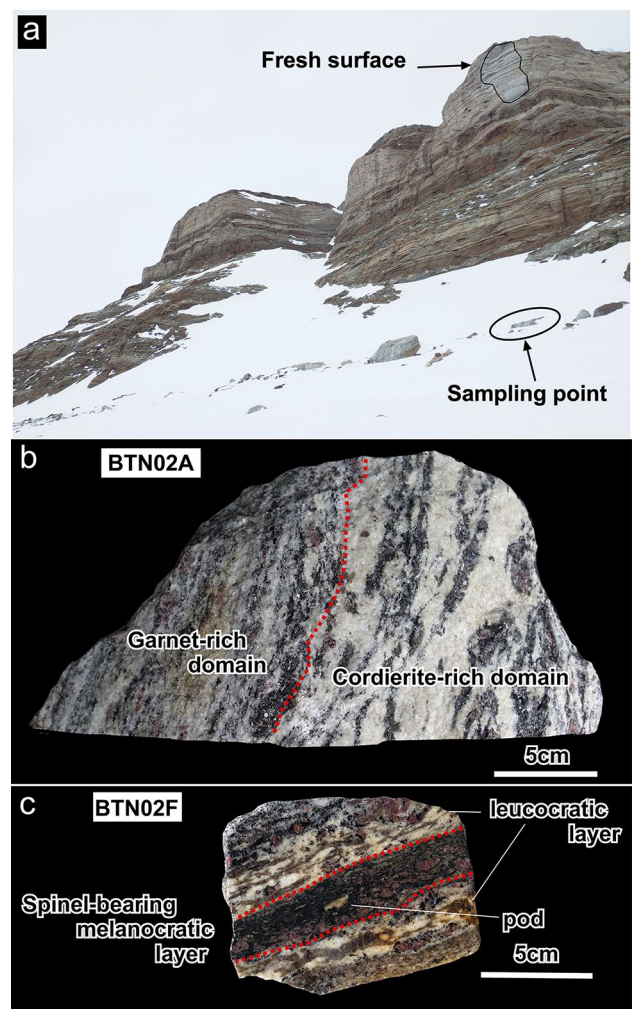


**Fig. 2** a Photograph of the northeast side of the Botnnuten. Higher side of the cliff has collapsed and shows fresh white surface; b and c Photographs of collected samples

conductive carbon to prevent charging. Pre-selected spots were analyzed in a JEOL JXA-8200 EPMA instrument. Analytical conditions were maintained at an accelerating voltage of 15 kV and a beam current of 12 nA for spot analyses and 150 nA for element mapping. The instrument was equipped with five wavelength-dispersive spectrometers (WDS), and all elements were measured at their respective  $K\alpha$  lines for 10 s on peak and 5 s on each upper and lower background. The used reference materials were wollastonite (Si), corundum (Al), periclase (Mg), hematite (Fe), spessartine (Mn), wollastonite (Ca), rutile (Ti), chromite (Cr), albite (Na), orthoclase (K), apatite (P, F). ZAF correction was applied to the analysis and corrected element contents were recalculated to weight percent. Total iron is reported as  $FeO_T$ .

## Whole rock composition

To determine the whole-rock chemical compositions of the samples, rock slabs of each sample, about  $50 \times 50 \times 10 \text{ mm}^3$  for BTN02A and  $25 \times 25 \times 10 \text{ mm}^3$  for BTN02F, were ground in a stainless-steel mortar to a particle size of  $\sim 2 \text{ mm}$ , and subsequently pulverized in a quartz ball mill using a Fritsch Pulverisette 6. Before fusion, all samples were heated at  $1000 \text{ }^\circ\text{C}$  for 2 h to remove volatiles and oxidize ferrous iron. Powdered samples ( $1.8000 \pm 0.0005 \text{ g}$ ) were thoroughly mixed with 2 $\times$  excess Li-metaborate and fused to form a glass bead in an induction furnace using a NT-2000 Bead Sampler (Tokyo-Kagaku Co., Ltd.) by heating in several stages: first at  $1200 \text{ }^\circ\text{C}$  for 2 min, and then swing heating at  $1200 \text{ }^\circ\text{C}$  for 6 min. Whole-rock element contents were determined in a RIGAKU RIX 2000 X-ray fluorescence spectrometer instrument equipped with an Rh-tube operated at 50 kV and 50 mA. The loss on ignition (LOI) was determined gravimetrically by placing the sample powder in a furnace at  $110 \text{ }^\circ\text{C}$  and  $1000 \text{ }^\circ\text{C}$ , and weighing the sample at each temperature. The instrument operating conditions of the XRF spectrometers are documented by Kimura and Yamada (1996).

## Phase equilibria modeling

To investigate the metamorphic conditions of a cordierite-bearing gneiss and spinel–garnet-bearing gneiss, a  $\text{Na}_2\text{O}$ – $\text{CaO}$ – $\text{K}_2\text{O}$ – $\text{FeO}$ – $\text{MgO}$ – $\text{Al}_2\text{O}_3$ – $\text{SiO}_2$ – $\text{H}_2\text{O}$ – $\text{TiO}_2$  (NCKFMASHT) and NCKFMASHTO (NCKFMASHT– $\text{O}_2$ )  $P$ – $T$  isochemical phase diagram was computed for each sample based on free-energy minimization using Perple\_X 6.8.7 software (Connolly 2005) and end-member thermodynamic data from Holland and Powell (2011) (filename: hp62ver.dat). The activity models of White et al. (2014) are used for orthopyroxene, biotite, garnet, cordierite, chlorite, mica, and staurolite, Wheller and Powell (2014) for sapphirine, White et al. (2002) for spinel, Fuhrman and Lindsley (1988) for feldspar, Holland et al. (2018) for melt and ideal solution models for ilmenite (IlGkPy). Details of these models and any modifications are given in the “Perple\_X solution model glossary” and “Perple\_X Updates” files, which are available at [http://www.perplex.ethz.ch/perplex\\_updates.html](http://www.perplex.ethz.ch/perplex_updates.html).

## Results

### Petrography and mineral chemistry

#### Cordierite-bearing gneiss (BTN02A)

The cordierite-bearing gneiss (sample BTN02A) occurs as compositional layers within predominantly

garnet–biotite–sillimanite gneisses (Fig. 2b). Sample BTN02A contains a cordierite-rich domain and a garnet-rich domain (Fig. 2b). The cordierite-rich domain (Fig. 2b) contains cordierite, biotite, sillimanite, K-feldspar, quartz, and plagioclase, with accessory zircon, ilmenite, and apatite. A small amount of garnet is also present. This domain is leucocratic with abundant feldspar-quartz layers that cross-cut the melanocratic lenses and layers. Cordierite megacrysts are up to 17 mm in diameter (Fig. 3a) and occur in localized clusters that are aligned with the gneissic banding (Fig. 2b). The cordierite is predominantly inclusion free, with rare biotite inclusions. The cordierite margins are partially replaced by biotite and subhedral–euhedral prismatic sillimanite (Fig. 3a). The  $X_{\text{Mg}}$  [molar Mg/(Mg+Fe)] value of cordierite decreases slightly from core (0.81) to rim (0.78) in a single analyzed crystal (Table 1 and Tables S1–S5). In places, garnet occurs alongside biotite at the margins of cordierite (Fig. 3b and c). Garnet crystals (up to 4 mm in size) are smaller than cordierite, and they have an irregular morphology with sharp crystal margins. The garnets have a narrow compositional range of pyrope (28–32 mol%), grossular (1.0–1.6 mol%), and spessartine (1.0–1.6 mol%; Fig. 4a and b). Biotite occurs predominantly at the cordierite margins and has  $X_{\text{Mg}}$  values of 0.55–0.62, and  $\text{TiO}_2$  contents of up to 6.2 wt% (Fig. 4c). K-feldspar, quartz, and plagioclase occur in the matrix and are of variable size. K-feldspar is perthitic and shows lamellae textures such as stringlets, rods, and interlocking lamellae. Plagioclase and K-feldspar have near-uniform compositions of anorthite ( $\text{An} = 14$ – $16 \text{ mol}\%$ ) and orthoclase ( $\text{Or} = 89$ – $93 \text{ mol}\%$ ), respectively (Fig. 5a).

The garnet-rich domain (Fig. 6) contains garnet, cordierite, biotite, sillimanite, plagioclase, K-feldspar and quartz, with accessory zircon, ilmenite, and apatite. Garnet occurs as porphyroblasts up to 8 mm in diameter, which are partially replaced by biotite and rarely by cordierite (Fig. 6a). Garnet porphyroblasts show a compositional range of pyrope (28–40 mol%), grossular (1.4–1.7 mol%), and spessartine (0.6–1.1 mol%). The pyrope contents of garnet are higher in the garnet-rich domain than in cordierite-rich domain, and are highest in the garnet cores. Cordierite occurs as isolated euhedral grains in the matrix (Fig. 6b), secondary grains replacing garnet (Fig. 6a), inclusions within garnet (Fig. 6c), and as grains that are partially surrounded by garnet (Fig. 6d). Cordierite grains adjacent to the garnet margins have higher  $X_{\text{Mg}}$  values (0.79–0.80) than other cordierite grains (0.74–0.78). Biotite in the garnet-rich domain has higher  $X_{\text{Mg}}$  ratios (0.70–0.59) than biotite in cordierite-rich domains, and biotite inclusions in garnet have similarly high  $X_{\text{Mg}}$  ratios (up to 0.70) and moderate F contents (up to 0.52 wt%; Fig. 4c). Plagioclase shows little compositional variation ( $\text{An} = 14$ – $15 \text{ mol}\%$ ).

**Table 1** Chemical compositions (EPMA results), and calculated mineral formulae and end-member fractions, for selected minerals

Sample	BTN02A(Crd-rich domain)					BTN02A(Grt-rich domain)			BTN02F			
	Spot No.	47	7	2	18	15	99	123	67	32	159	28
		Grt	Crd	Bt	Pl	Kfs	Grt	Crd	Bt	Grt	Spl	Pl
Major oxides (wt%):	LLD	C marg		in Crd			rim	G marg	G marg	core	Spl in Sil	
SiO <sub>2</sub>	0.02	38.92	50.00	36.30	65.12	64.82	38.25	49.71	36.19	37.75	0.06	61.38
TiO <sub>2</sub>	0.03	0.01	0.00	6.13	0.04	0.07	0.03	0.03	5.62	0.00	0.00	0.00
Al <sub>2</sub> O <sub>3</sub>	0.02	21.89	33.28	16.38	22.41	18.99	21.62	33.68	15.74	21.56	58.43	24.50
Cr <sub>2</sub> O <sub>3</sub>	0.03	0.08	0.02	0.14	0.01	0.00	0.04	0.03	0.15	0.00	0.32	0.00
FeO <sup>T</sup>	0.05	30.20	4.97	15.37	0.01	0.00	31.60	4.75	17.31	33.06	37.16	0.02
MnO	0.04	0.59	0.00	0.00	0.01	0.00	0.51	0.00	0.00	0.96	0.04	0.05
MgO	0.01	8.45	10.46	12.10	0.02	0.00	7.23	10.49	11.34	5.24	3.86	0.00
CaO	0.01	0.48	0.01	0.04	3.31	0.05	0.52	0.02	0.08	1.35	0.02	5.86
Na <sub>2</sub> O	0.02	0.00	0.05	0.11	9.76	1.25	0.02	0.01	0.11	0.05	0.03	8.23
K <sub>2</sub> O	0.01	0.01	0.02	9.66	0.16	15.07	0.01	0.01	9.69	0.01	0.00	0.20
ZnO	0.01	-	-	-	-	-	-	-	-	-	0.21	-
Total		100.63	98.81	96.22	100.85	35.42	99.82	98.73	96.22	99.97	100.12	38.86
Calculated mineral formulae (apfu) <sup>a</sup>												
O		12	18	22	8	8	12	18	22	12	4	8
Si		3.003	5.037	5.392	2.846	2.976	2.999	5.007	5.432	2.991	0.002	2.720
Ti		0.001	0.000	0.684	0.001	0.002	0.002	0.002	0.634	0.000	0.000	0.000
Al		1.991	3.952	2.867	1.154	1.028	1.998	3.998	2.784	2.013	1.944	1.280
Cr		0.005	0.001	0.016	0.000	0.000	0.003	0.002	0.018	0.000	0.007	0.000
Fe <sup>3+</sup>		-	-	-	0.000	0.000	-	-	-	0.013	0.047	0.001
Fe <sup>2+</sup>		1.948	0.419	1.909	-	-	2.073	0.400	2.173	2.177	0.830	-
Mn		0.039	0.000	0.000	0.000	0.000	0.034	0.000	0.000	0.064	0.001	0.002
Mg		0.971	1.571	2.680	0.001	0.000	0.844	1.574	2.537	0.619	0.163	0.000
Ca		0.039	0.001	0.006	0.155	0.002	0.043	0.002	0.013	0.114	0.000	0.278
Na		0.000	0.009	0.030	0.827	0.112	0.003	0.003	0.032	0.008	0.002	0.707
K		0.001	0.003	1.830	0.009	0.882	0.001	0.001	1.854	0.001	0.000	0.011
Zn		-	-	-	-	-	-	-	-	-	0.004	-
Sum		7.998	10.992	15.413	4.994	5.003	8.000	10.989	15.476	8.000	3.000	4.999
X <sub>Mg</sub>		0.33	0.79	0.58			0.29	0.80	0.54	0.22	0.16	
Calculated end-member fractions (mol%):												
Grossular		1.32					1.45			3.85		
Pyrope		32.40					28.20			20.81		
Spessartine		1.29					1.14			2.15		
Almandine		64.99					69.21			73.18		
X <sub>An</sub>					0.16	0.00						0.28
X <sub>Zn</sub>											0.00	

LLD Lower limit of detection, FeO<sup>T</sup> represents total iron oxide, Fe<sup>3+</sup> is calculated based on charge balance

C marg in marginal part of cordierite (Crd), G marg in marginal part of garnet (Grt)

X<sub>Mg</sub> = Mg/(Mg+Fe), X<sub>An</sub> = Ca/(Na+Ca+K), X<sub>Zn</sub> = Zn/(Zn+Mg+Fe<sup>2+</sup>)

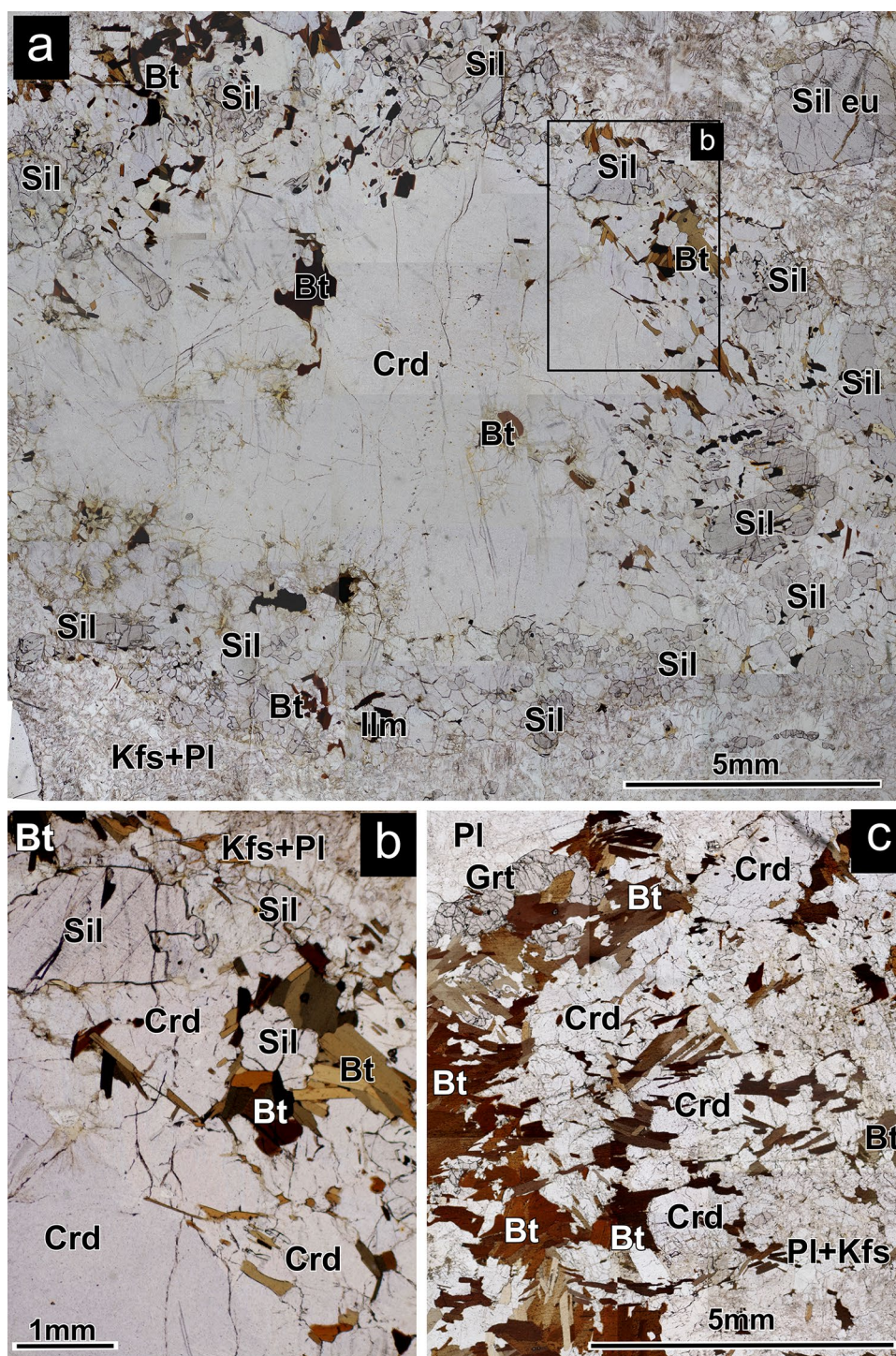
<sup>a</sup>Calculated based on the quoted number of O atoms per formula unit

### Spinel–garnet-bearing gneiss (BTN02F)

Spinel–garnet-bearing gneiss (sample BTN02F) occurs as melanocratic layers within predominantly garnet–biotite gneiss and exhibits a grano–porphyroblastic texture.

The melanocratic layer contains garnet, spinel, biotite, plagioclase, and K-feldspar, with subordinate corundum and sillimanite, and accessory zircon, ilmenite, rutile, and apatite. Quartz, plagioclase, and K-feldspar can be seen in the leucocratic layer adjacent to the melanocratic

**Fig. 3** Plane-polarized transmitted-light photomicrographs of a cordierite porphyroblast in cordierite-rich domain in sample BTN02A (cordierite gneiss); **a** Large cordierite (Crd) porphyroblast in domain (i). Sillimanite (Sil) and biotite (Bt) occur at the cordierite margin. Euhedral sillimanite (Sil eu) occurs in the matrix; **b** Enlarged photomicrographs of the cordierite margin; **c** Cordierite margin is replaced by biotite (Bt). Garnet (Grt) is present with Bt. Pl = Plagioclase, Kfs = alkali feldspar, Ilm = ilmenite



layer (Fig. 2c). The leucocratic layer partially invades the melanocratic layer and occurs as pods (Fig. 2c). In the melanocratic layer, garnet occurs as porphyroblasts up to 8 mm in diameter. The garnet contains scarce inclusions of biotite, spinel, ilmenite, and plagioclase that are small and rounded (Fig. 7a). Garnet locally occurs as overgrowths on spinel rims (Fig. 7a). Spinel occurs as granular crystals in the matrix of the gneiss (Fig. 7a

and b) and is weakly foliated, together with plagioclase. Small inclusions of spinel occur within garnet, sillimanite, and corundum (Fig. 7a, c, and d). Spinel grains in the matrix and included spinel have  $X_{Mg}$  values of 0.16–0.24 (Fig. 5b). Spinel ZnO contents are <0.35 wt% and the  $Fe^{3+}$  content calculated by charge balance is <0.07 apfu ( $O=4$ ). The biotite is finer-grained than the spinel and the garnet, and occurs as crystal aggregates (Fig. 7c) with

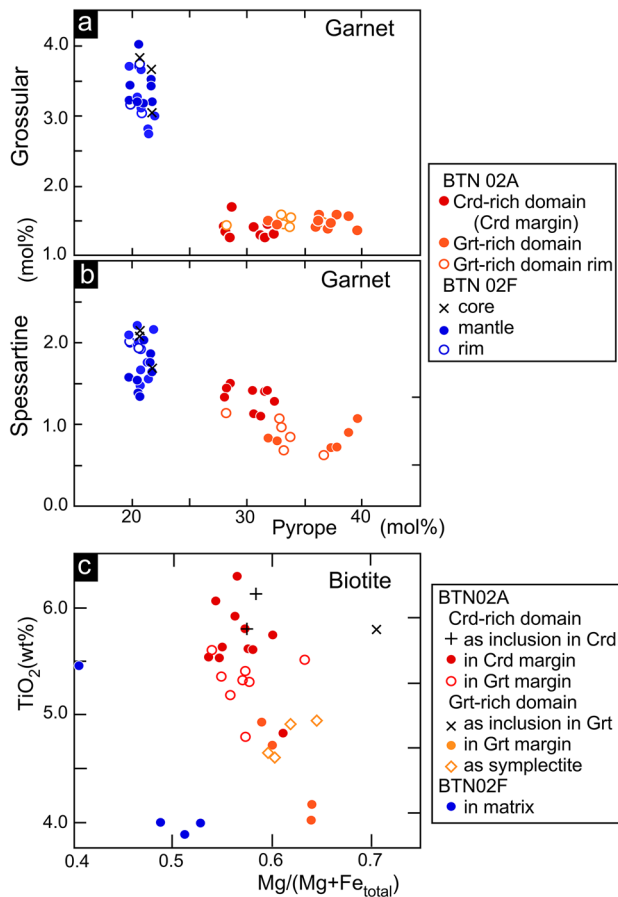


**Fig. 4** **a** and **b** Compositional variations of garnet in terms of pyrope versus grossular and pyrope versus spessartine; **c** Compositional variations of biotite in terms of  $X_{Mg}$  versus  $TiO_2$  contents. Grossular =  $Ca/(Mg+Fe+Ca+Mn) \times 100$ , Spessartine =  $Mn/(Mg+Fe+Ca+Mn) \times 100$ , Pyrope =  $Mg/(Mg+Fe+Ca+Mn) \times 100$

$X_{Mg}$  ratios and  $TiO_2$  contents of 0.40–0.53 and 3.9–5.5 wt%, respectively (Fig. 4c). Sillimanite and corundum occur together in the matrix with spinel. Corundum occurs as irregularly shaped crystals in the matrix and contains inclusions of spinel and ilmenite (Fig. 7b and c). Sillimanite occurs as euhedral to subhedral grains that contain inclusions of spinel and corundum (Fig. 7c). Locally, biotite replaces corundum and sillimanite at their grain margins. Sillimanite and corundum have  $Fe_2O_3$  contents up to 0.43 wt% and 0.41 wt%, respectively. Plagioclase is uniform in size, has a granoblastic texture, and has a narrow range of anorthite contents (27–29 mol%; Fig. 5a). K-feldspar is perthitic and contains fine lamellae, is less abundant than plagioclase, and has a wide range of orthoclase contents (Or = 65–90 mol%).

## Pseudosection modeling

### General remarks

Pseudosection modelings, NCKFMASHT and NCKFMASHTO, were used to determine the  $P$ – $T$  conditions recorded by the cordierite-rich domain in sample BTN02A, and by the spinel–garnet-bearing melanocratic layer in sample BTN02F. To calculate the pseudosections,  $H_2O$  contents were determined from LOI values, and whole-rock compositions were normalized to a total of 100 wt%. The analytical results of whole-rock compositions are presented in Table S6. Three types of models were calculated 1) a model based on whole-rock composition by XRF disregarding the oxidation state (Model WR), 2) a model based on whole-rock by XRF composition with an assumed oxidation state (Model WR+O), and 3) a model calculated from the composition of the large cordierite with surrounding sillimanite (Fig. 3a) assuming an effective domain composition with different  $H_2O$  (Model Crd-domain). The Model WR is based on analytical data, whereas the Model WR+O and the Model Crd-domain involved assumptions to estimate  $Fe_2O_3$  and  $H_2O$ . Each model is discussed individually in the following sections.

### Model WR - sample BTN02A

We estimated the whole-rock compositions by XRF analysis of cordierite-rich domains from sample BTN02A, and applied them to the modeling of pseudosections (Fig. 8a). Sample BTN02A shows a leucocratic appearance with discontinuous melanocratic layers and lenses cross-cut by leucocratic layers. Based on 6000 point counts from three thin sections, domain contain 29 vol% plagioclase, 28 vol% K-feldspar, 24 vol% cordierite, 8 vol% biotite, 7 vol% sillimanite, 3 vol% garnet, 1 vol% quartz, and 0.2 vol% ilmenite. The inferred peak mineral assemblage for this sample is cordierite–biotite–sillimanite–garnet–plagioclase–melt  $\pm$  quartz, which is stable on the calculated pseudosection (Fig. 8a) at 6–7 kbar and 780–850 °C. The measured modal proportion of cordierite in this sample (24 vol%) is modelled to occur only at low- $P$  and high- $T$  conditions of <5 kbar and 770–850 °C. However, the measured modal abundance of garnet (3 vol%) is modelled to occur at high- $P$ , at ~6.5–7.1 kbar. The measured modal abundance of sillimanite (7 vol%) is modelled to occur at low- $P$  and high- $T$  conditions of <6 kbar, 775–850 °C, and is located outside of the modelled peak  $P$ – $T$  conditions. The calculated modal abundance of sillimanite increases toward low- $T$  and high- $P$  conditions, whereas that of garnet increases toward high- $P$  and high- $T$  conditions (Fig. 8a).



**Model WR - sample BTN02F**

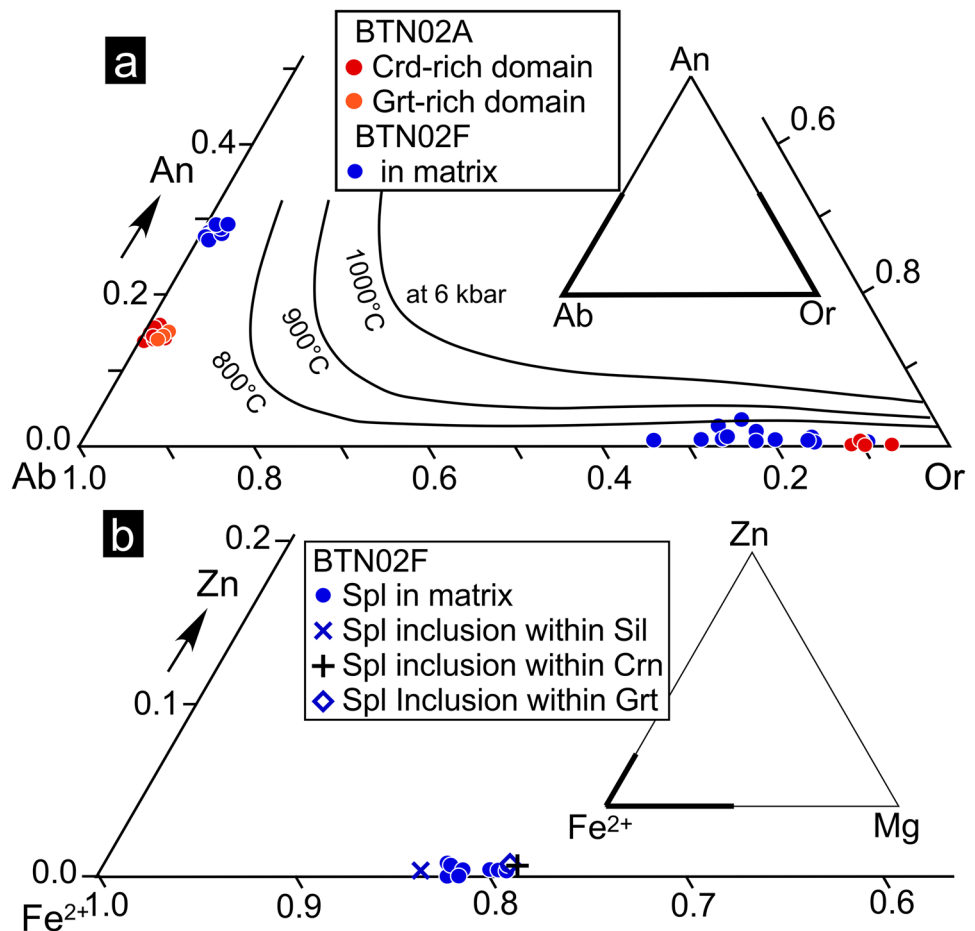
This sample contains plagioclase (33 vol%), K-feldspar (28 vol%), garnet (17 vol%), spinel (11 vol%), biotite (6 vol%), sillimanite (2 vol%), corundum (1 vol%) and ilmenite (1 vol%). The presence of a small amount of melt is assumable from the leucocratic layer partially invading into the melanocratic layer and occurring as pods (Fig. 2c). The inferred peak mineral assemblage for this sample is garnet-spinel-plagioclase-K-feldspar-ilmenite-melt, which is stable on the modelled pseudosection (Fig. 8b) at 4.5–8.0 kbar and 830–900 °C. The observed mineral assemblage (inferred peak minerals plus biotite-sillimanite-corundum) is stable at 6.2 kbar and 800 °C. The measured modal abundance of spinel (11 vol%) and garnet (17 vol%) suggest low- $P$  (<4.5 kbar) and high- $T$  (750–900 °C) conditions based on the positions of the calculated modal proportion isopleths (Fig. 8b). The calculated isopleth for the estimated modal proportion of garnet (17 vol%) is located at ~4.5 kbar, where it intersects mineral assemblage characterized by stable cordierite or orthopyroxene, neither of which are present in the assemblage observed in the sample. In

contrast, the measured modal abundance of sillimanite (2 vol%) and corundum (1 vol%) suggest  $P$ - $T$  conditions of <6 kbar and 780–800 °C.

**Model WR+O - sample BTN02A**

We assessed the bulk-rock oxidation state using  $Fe_2O_3$  estimated from average biotite and garnet compositions. A biotite  $Fe^{3+}/(Fe^{3+} + Fe^{2+})$  value of 0.08 was applied, based on the typical composition of granulite-facies biotite (Stephenson 1977; Deer et al. 1992), and a garnet  $Fe^{3+}/(Fe^{3+} + Fe^{2+})$  value of 0.02, which was estimated from charge balance calculations. The bulk-rock oxidation state was assumed to be  $Fe_2O_3:FeO=0.02:2.19$ , obtained from modal mineral proportions and average mineral  $Fe^{3+}$  compositions, according to Palin et al. (2016). In Fig. 9a shows the pseudosection incorporating the estimated  $Fe_2O_3$  content (as “ $O_2$ ”). The pseudosection topology is near-identical to that calculated for Model WR (Fig. 8a), except for the addition of spinel-stable fields. The inferred peak assemblage is stable on the calculated pseudosection (Fig. 9a) at 6.0–7.2 kbar and 750–850 °C, which is nearly the same as in the WR Model (Fig. 8a).

**Fig. 5** **a** Compositional variation of feldspar in terms of An-Ab-Or ternary diagrams. Ternary miscibility gaps are calculated for  $P=6$  kbar using the methods of Fuhrman and Lindsley (1988) and Wen and Nekvasil (1994); **b** Compositional variations of spinel (hercynite) in Fe-Mg-Zn ternary diagrams. Spinel included within sillimanite have lower  $X_{Mg}$  than in other textural settings. Spinel in sample BTN02F (Spl-Grt gneiss) have low ZnO contents



### Model WR+O - sample BTN02F

The modal proportions of spinel, garnet, and biotite and their average  $\text{Fe}^{3+}/(\text{Fe}^{3+} + \text{Fe}^{2+})$  compositions were used to estimate  $\text{Fe}_2\text{O}_3$  contents of this sample. The  $\text{Fe}^{3+}/(\text{Fe}^{3+} + \text{Fe}^{2+})$  ratios for spinel and biotite were estimated to be 0.06 and 0.10, respectively, and the whole-rock  $\text{Fe}_2\text{O}_3$  is inferred to be 0.57 wt% (0.25 mol%). The  $\text{Fe}^{3+}$  content of the garnet was found to be negative using an average composition, and based on the charge balance. Figure 9b shows a pseudosection for sample BNT02F incorporating  $\text{Fe}_2\text{O}_3$  (as  $\text{O}_2$ ). This pseudosection has a different topology to that for the Model WR (Fig. 8b). Spinel stability is restricted to both low- $P$  and high- $T$  conditions (Fig. 9b), whereas the sillimanite stability field is expanded.

The inferred peak mineral assemblage for this sample is garnet–spinel–plagioclase–K-feldspar–ilmenite–melt, which is stable on modeled pseudosection (Fig. 9b) at < 5.0–7.0 kbar and 800–900 °C. The observed mineral assemblage (inferred peak minerals plus biotite–sillimanite–corundum) is stable at  $\sim 6.1 \pm 0.1$  kbar and  $\sim 800 \pm 10$  °C (open circle in Fig. 9b). A calculated isopleth of the modal abundance of spinel (11 vol%) is located at 6.1 kbar and 870 °C in the melt–garnet–plagioclase–K-feldspar–ilmenite–spinel field (Fig. 9b) and is assumed to be peak conditions. On the calculated pseudosection (Fig. 9b), sillimanite is stable at 6.1 kbar and < 850 °C, whereas corundum is only stable at 6.1 kbar and < 800 °C. The stability fields of the spinel shift to spinel + sillimanite toward low- $T$  conditions. Spinel + sillimanite is further changed to sillimanite + corundum towards low- $T$

condition. The modal abundance of sillimanite (2 vol%) and corundum (1 vol%) are also modeled to stable at 6.1 kbar and 800 °C (open circle in Fig. 9b). The spinels were found in the matrix as inclusions of sillimanite and corundum (Fig. 7a and b). The mineral textural relationships indicate that the spinel was stable first, followed by the growth of sillimanite and corundum. This implies that the rock transversed the IBC  $P$ – $T$  path from the spinel stability field toward the stability fields of spinel + sillimanite, and subsequently corundum + sillimanite (see arrow in Fig. 9b).

### Model Crd-domain - sample BTN02A

This model is only applied to BTN02A to evaluate the texture observed in large cordierite and surrounding sillimanite (Fig. 3a). This rock exhibits a heterogeneous appearance (Fig. 2a), with large cordierite appearing as melanocratic lenses in the cordierite-rich domain. This led us to perform a pseudosection calculation based on the bulk composition of the domain. Domain composition is calculated by assuming sphere cordierite (10 mm in diameter) in a cube matrix (15  $\text{mm}^3$ ). The mineral mode of cordierite (16 vol%) and matrix (84 vol%) was calculated. The mineral mode of the matrix was estimated using point counts, except for cordierite, in large cordierite-bearing thin sections (Fig. 3a).

The estimated domain contains 31 vol% plagioclase, 32 vol% K-feldspar, 16 vol% cordierite, 4 vol% biotite, 16 vol% sillimanite, 1 vol% quartz, and 1 vol% ilmenite. Average mineral compositions by EPMA and modal proportions of minerals are applied to estimate domain composition

**Fig. 6** Plane-polarized transmitted-light photomicrographs of garnet-rich domain in sample BTN02A (cordierite-felsic gneiss). **a** Garnet (Grt) porphyroblast is partially replaced by biotite (Bt) and cordierite (Crd); **b** Euhedral cordierite surrounded by biotite in the matrix; **c** cordierite is completely and partially surrounded by garnet. The garnet margin was not replaced by cordierite; **d** Cordierite surrounded by the irregular shaped garnet which shows a sharp crystal margin. Qz = quartz

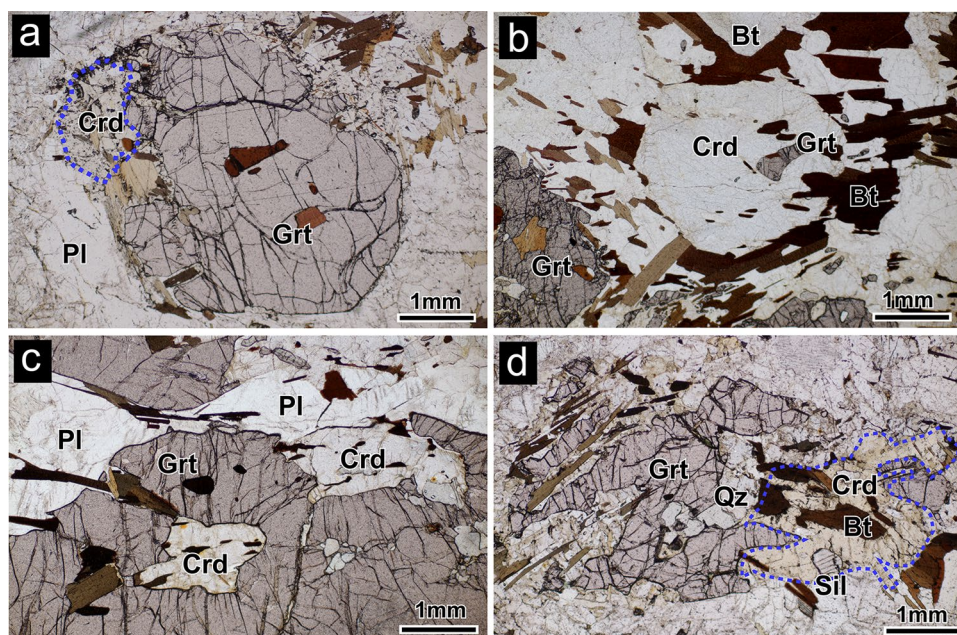
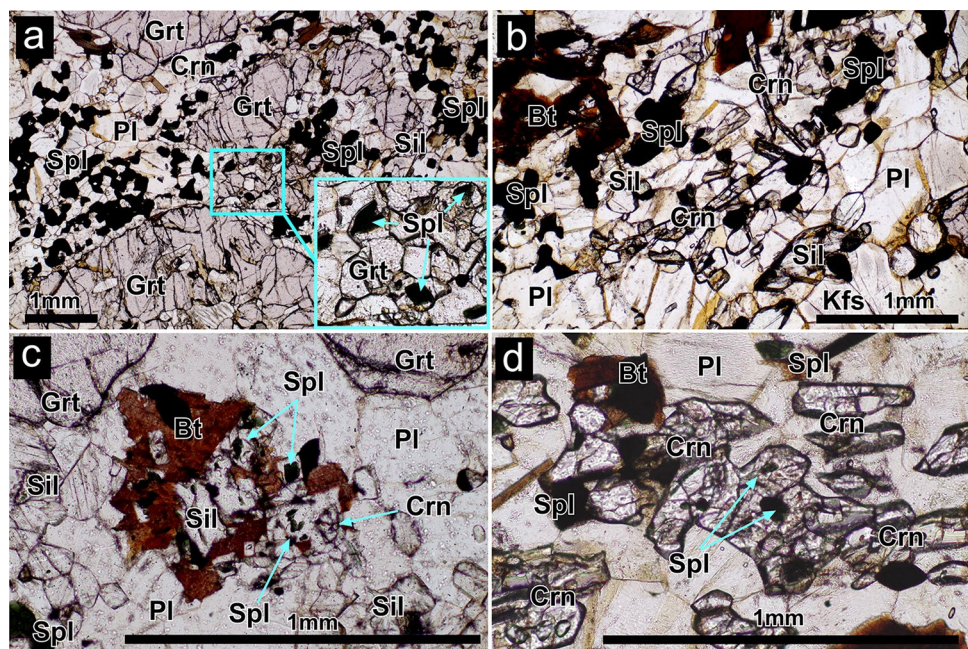


**Fig. 7** Plane-polarized transmitted-light photomicrographs showing mineral relationships in sample BTN02F (spinel-garnet gneiss). **a** Garnet porphyroblast and spinel (Spl) in a matrix of plagioclase (Pl). Closeup view of spinel enclosed by thin garnet; **b** Corundum (Crn) and sillimanite (Sil) occur in the matrix; **c** Sillimanite contains micro-inclusions of spinel and corundum and is surrounded by biotite; **d** Corundum contains spinel inclusions



according to Palin et al. (2016). The  $H_2O$  contents were inferred from the LOI values because the estimated  $H_2O$  from modal proportions of mineral was low (0.28 wt%), and the preliminary calculation gave unrealistic pseudosection results involving orthopyroxene and a wide spinel stability field. Two models of all LOI as  $H_2O$  (1.0 LOI) and half LOI as  $H_2O$  (0.5 LOI) were applied. Figure 10 shows the results of the two models. The inferred peak mineral assemblage for this domain is biotite–cordierite–plagioclase–K-feldspar–sillimanite–melt, which is stable on the calculated pseudosection at 4.0–6.5 kbar and 720–840 °C (Model  $H_2O$  = 1.0 LOI, Fig. 10a) and at 5.8–6.2 kbar and 780–840 °C (Model  $H_2O$  = 0.5 LOI, Fig. 10b). The calculated modal abundance isopleths of cordierite (16 vol%) and sillimanite (16 vol%) suggest low- $P$  (4.9–5.2 kbar) and high- $T$  (830–840 °C) in both models (stars in Fig. 10a and b) are located outside of stability field of inferred peak assemblage. The inferred  $P$ - $T$  condition of ~5.2 kbar and ~840 °C estimated from isopleth in Model  $H_2O$  = 0.5 LOI is located in spinel–corundum  $\pm$  sapphirine stable fields, which is inconsistent with our petrographic observation. The inferred  $P$ - $T$  condition of ~4.9 kbar and ~830 °C, respectively, estimated from isopleths in Model  $H_2O$  = 1.0 LOI is located at the melt–biotite–cordierite–plagioclase–K-feldspar–sillimanite–rutile stable field. Rutile was not present in the measured domain, but was almost the same as the inferred peak assemblage. Therefore, this model is considered more reliable. Euhedral to subhedral sillimanite is present in the matrix and the cordierite margin (Fig. 3a), and the cordierite does not contain sillimanite inclusions. These sillimanites are interpreted to have crystallized in a late phase compared

to cordierite. As the modal abundance of sillimanite in the Model  $H_2O$  = 1.0 LOI increases toward high- $P$  and low- $T$ , sillimanites may crystallize during cooling, crossing the isopleths (gray arrow in Fig. 10a).

## Discussion

### Metamorphic $P$ - $T$ path

#### Sample BTN02A

Previous studies have described cordierite from Sinnan Rock and Cape Ryugu, which are located within the amphibolite-facies zone in the eastern part of the LHC (Shiraishi et al. 1989). Secondary cordierite has been identified in rocks along the southern part of the Soya Coast at Rundvågshetta, occurring as decompression-related corona textures consisting of cordierite + orthopyroxene and cordierite + sapphirine (Ishikawa et al. 1994; Motoyoshi and Ishikawa 1997; Yoshimura et al. 2008). However, no studies have reported large porphyroblasts of cordierite, and the sample described here is presumed to contain the largest cordierite grains known in the LHC.

Cordierite occurs as variably shaped, subhedral to irregular grains within the different textural domains of sample BTN02A. In cordierite-rich domains, large cordierite porphyroblasts contain biotite inclusions and are in contact with biotite within the matrix (Fig. 6b). The biotite inclusions within cordierite and biotite in the matrix have high  $TiO_2$  contents (~6.1 wt%), suggesting crystallization

## Model WR

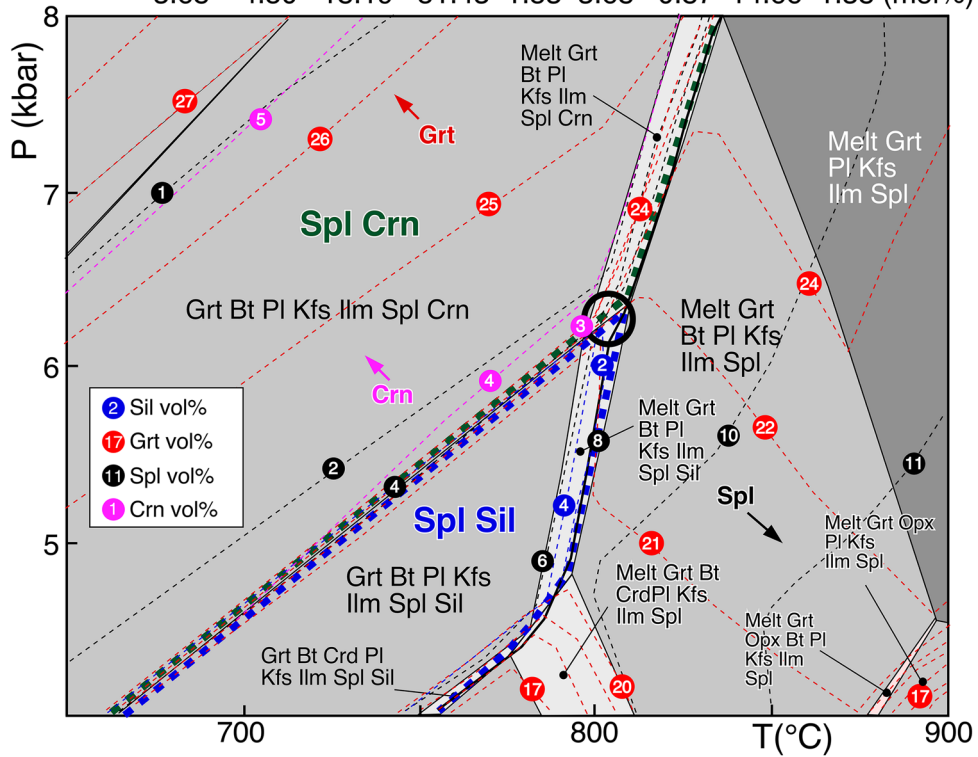
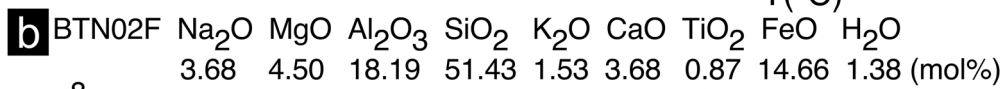
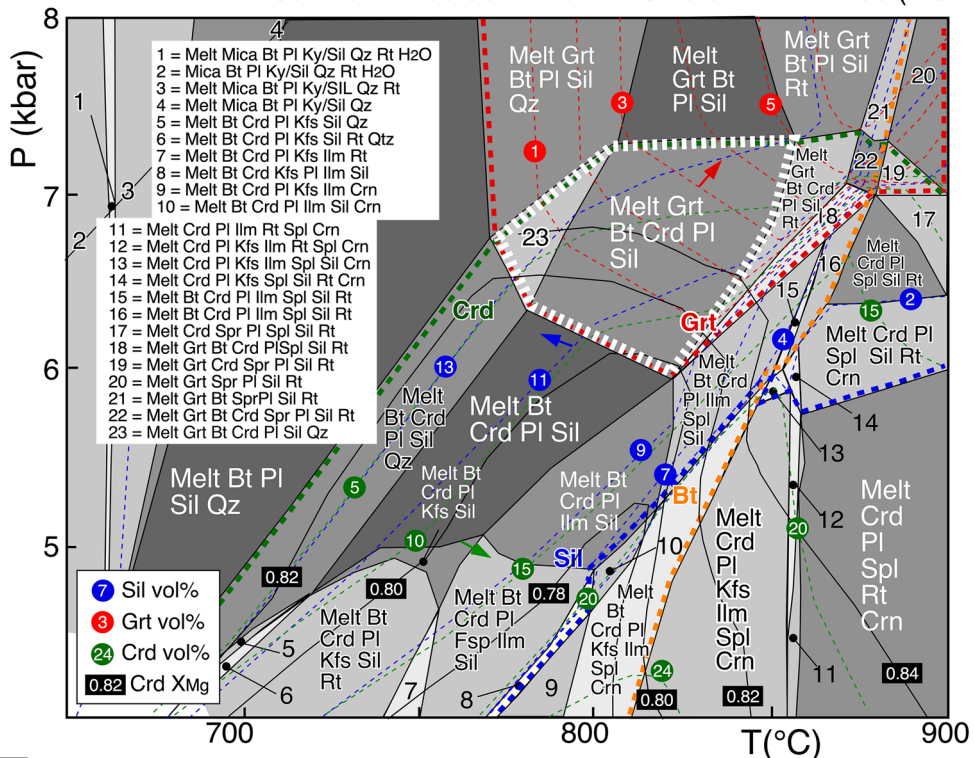
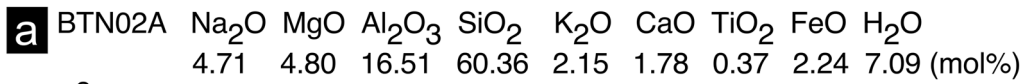


**Fig. 8** NCKFMASHT  $P$ – $T$  pseudosection using the whole-rock composition (Model WR). **a** Result of the cordierite-rich domain of BTN02A. Modal abundance isopleths are shown for garnet, sillimanite, cordierite, and isopleths of  $[X_{Mg} = Mg/(Mg + Fe)]$  cordierite are shown. Small arrows represent an increased trend of a modal abundance of each mineral with the same color as isopleths. The white dashed area represents a stable field of the mineral assemblage of melt-garnet-biotite-cordierite-plagioclase-sillimanite  $\pm$  quartz. **b** Result of the of BTN02F. Modal abundance isopleths are shown for garnet, sillimanite spinel and corundum. Open circle represents condition of the mineral assemblage for melt-garnet-biotite-spinel-corundum-sillimanite-plagioclase-K-feldspar-ilmenite. Bt=biotite, Crn=corundum, Grt=garnet, Ilm=ilmenite, Kfs=K-feldspar, Ky=kyanite, Pl=plagioclase, Qz=quartz, Rt=rutile, Spl=spinel, Spr=sapphirine

under high- $T$  conditions. Considering the estimated modal proportion (24 vol%) and  $X_{Mg}$  values ( $\sim 0.81$ ) of cordierite and the position of these isopleths in Model WR and Model WR+O, this phase was likely stable at the peak- $T$  conditions of  $\sim 4.5$  kbar and  $\sim 825$  °C. The estimated conditions located in the spinel and corundum stable fields were inconsistent with those of sample BTN02A, which did not contain either spinel or corundum. Otherwise, inferred pressure values using modal proportion of garnet (3 vol%) suggests 6.5–7.1 kbar but the modal proportion is low. In addition, the estimated peak  $P$ – $T$  fields (white dashed area in Fig. 8a and b) lacked K-feldspar. Therefore, the estimated conditions are uncertain.

In the case of Model Crd domain, the modal abundance isopleths of cordierite and sillimanite indicate 5 kbar and 830 °C in the  $H_2O = 1.0$  LOI model, which is more appropriate than the 0.5 LOI model. In the 0.5 LOI model, spinel, corundum, and sapphire are stable at the inferred  $P$ – $T$  condition using a modal abundance (Fig. 10b). Sillimanite is typically a late phase, as it is not commonly found as inclusions in large cordierite. Euhedral to subhedral sillimanite and biotite crystallization on the margins of the large cordierite may have progressed during cooling, which is consistent with the increased modal abundance of sillimanite and decreased cordierite (Fig. 10a). The late crystallization of sillimanite occurred within the melt–biotite–cordierite–plagioclase–K-feldspar–sillimanite stability field during cooling after the peak conditions (gray arrow in Fig. 10a). As isopleths of a modal abundance of sillimanite and cordierite have low-angle positive  $dT/dP$  slope, a slight increase in pressure during IBC is likely.

One of the main lines of evidence for an IBC  $P$ – $T$  path for the Botnnuten gneiss is the growth of euhedral to subhedral sillimanite and biotite at the margins of cordierite in the sample BTN02A (Fig. 3a). The cordierite contains high-TiO<sub>2</sub> biotite and lacks sillimanite inclusions. Similar textural relationships, in which cordierite is overgrown by fine-grained biotite+sillimanite $\pm$ ilmenite, has been reported

in granulite-facies metapelite from the Rayner Complex, and has been interpreted to reflect a near-IBC path or a counter-clockwise  $P$ – $T$  trajectory (MacRobertson Land and Northern Prince Charles Mountains; Clarke et al. 1989; Boger and White 2003; Halpin et al. 2007).

### Sample BTN02F

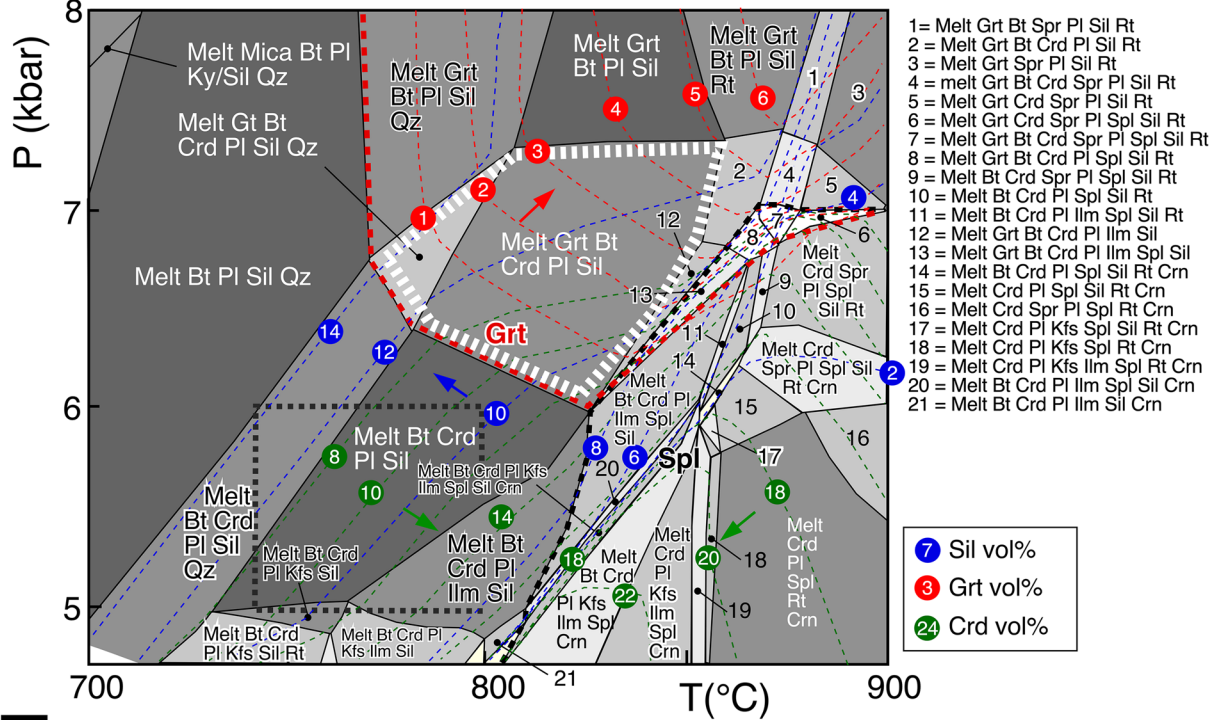
In the spinel-garnet-bearing gneiss (sample BTN02F), spinel is of consistent size and is abundant throughout the matrix. As the spinel does not contain significant ZnO, it is unlikely to be a product of the breakdown of staurolite; thus, the spinel-forming reaction remains unclear. Sillimanite and corundum occur together in the matrix with spinel, and garnet locally occurs as overgrowths on spinel rims (Fig. 7a). Sillimanite and corundum often contain spinel and coexist with biotite in the matrix (Fig. 7c), suggesting they crystallized after spinel together with biotite. Phase relations obtained from Model WR+O incorporating O<sub>2</sub> (Fig. 9b) show a different topology than the Model WR ignoring O<sub>2</sub> (Fig. 8b). It implies that the oxidation state is an essential factor in elucidating the stability field of spinel. Boger et al. (2012) calculated a pseudosection considering Fe<sub>2</sub>O<sub>3</sub> for spinel-bearing granulites, and their results showed the same phase relations as obtained in the present study, with spinel being stable under low- $P$  and high- $T$  conditions, and sillimanite under high- $P$  and low- $T$  conditions; therefore, we consider our  $P$ – $T$  estimate using Model WR+O to be reliable. The consumption of spinel to form corundum, sillimanite, and biotite is consistent with an IBC path from  $\sim 6.1$  kbar and  $\sim 870$  °C toward the garnet–corundum–sillimanite–spinel–biotite–K-feldspar–ilmenite–melt stability field (at  $\sim 6.2$  kbar and 800–810 °C) as shown in Model WR+O (Fig. 9b).

### Comparison with previous works

Motoyoshi and Shiraishi (1985) used phase relations and geothermobarometry to infer metamorphic  $P$ – $T$  conditions of 5–6 kbar and 750–800 °C for samples collected from Botnnuten by the First Japanese Antarctic Research Expedition in 1957. Their geothermobarometric results (dashed gray square in Fig. 9a) are consistent with the results of our modeling, and they likely represent the conditions during peak metamorphism. Although these  $P$ – $T$  conditions are similar to those of the Yamato–Belgica Complex (metamorphic age of 539 Ma; Shiraishi et al. 2003), located  $\sim 250$  km southwest of the LHC (Fig. 1b), Motoyoshi and Shiraishi (1985) concluded that Botnnuten is a low-pressure part of the LHC based on the occurrence of sillimanite, and geothermobarometric results (garnet–biotite, two-pyroxene and garnet–orthopyroxene geothermometries

Model WR+O

**a** BTN02A\_O  
 Na<sub>2</sub>O MgO Al<sub>2</sub>O<sub>3</sub> SiO<sub>2</sub> K<sub>2</sub>O CaO TiO<sub>2</sub> FeO H<sub>2</sub>O O<sub>2</sub> (mol%)  
 4.712 4.798 16.512 60.347 2.148 1.780 0.366 2.207 7.096 0.004



**b** BTN02F\_O  
 Na<sub>2</sub>O MgO Al<sub>2</sub>O<sub>3</sub> SiO<sub>2</sub> K<sub>2</sub>O CaO TiO<sub>2</sub> FeO H<sub>2</sub>O O<sub>2</sub> (mol%)  
 3.70 4.45 18.28 51.68 1.51 3.64 0.88 14.19 1.38 0.05

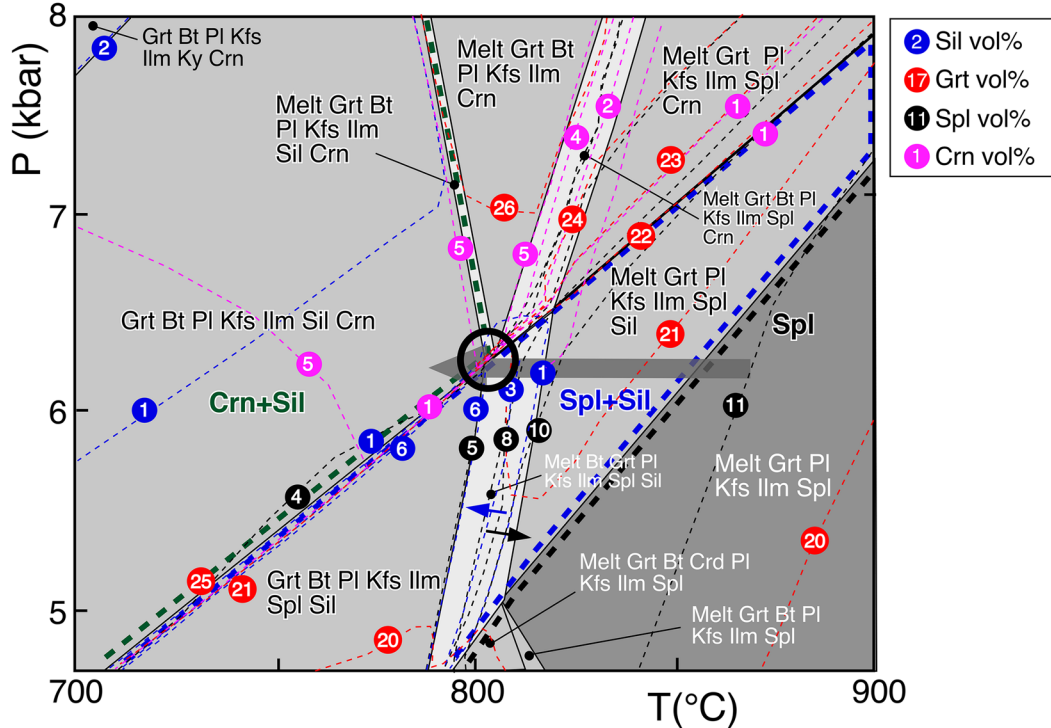


**Fig. 9** NCKFMASHTO  $P$ – $T$  pseudosection using the whole-rock composition (Model WR+O). **a** Result of the cordierite-rich domain of BTN02A. Modal abundance isopleths are shown for garnet, sillimanite and cordierite. The white dashed area represents a stable field of the mineral assemblage of melt-garnet-biotite-cordierite-plagioclase-sillimanite  $\pm$  quartz. The dashed square represents the  $P$ – $T$  condition for Botnnuten estimated by Motoyoshi and Shiraiishi (1985). **b** Result of the of BTN02F. Modal abundance isopleths are shown for garnet, sillimanite spinel and corundum. Open circle represents condition of the mineral assemblage of melt-garnet-biotite-spinel-corundum-sillimanite-plagioclase-K-feldspar-ilmenite. The arrow indicates the inferred  $P$ – $T$  path from the point modal abundance isopleth spinel (11 vol%) to the open circle

and garnet–plagioclase–orthopyroxene/clinopyroxene–quartz geobarometries). Despite the absence of staurolite, they assumed a staurolite break-down reaction and a prograde metamorphic history based on the occurrence of spinel.

The ITD-related orthopyroxene–plagioclase symplectite textures that characterize the other parts of LHC have not been identified in the mafic gneisses at Botnnuten. Previous studies of the  $P$ – $T$  conditions at Rundvågshetta, which is part of the high-grade section of the LHC, yielded maximum pressures of 13–15 kbar and  $\sim$ 900–1000 °C, during the early stages of metamorphism at ca. 580–520 Ma (Kawasaki et al. 2011; Hiroi et al. 2019; Dunkley et al. 2020), which are associated with an ITD path during the retrograde stage. The estimated pressure conditions are much higher than those estimated for Botnnuten in the present study. However, these UHT granulites occur as blocks and thin layers that are restricted to a narrow zone 250–500 m wide in north Rundvågshetta (Motoyoshi and Ishikawa 1997; Yoshimura et al. 2008; Hiroi et al. 2019). Tsunogae et al. (2014) estimated the metamorphic conditions of orthopyroxene-bearing orthogneiss exposed widely in south Rundvågshetta to be  $<$ 870 °C,  $<$ 9 kbar, and pointed out that the UHT is a local high-temperature event. Thus, the presence of a thickened crust along the entire LHT due to collision is questionable.

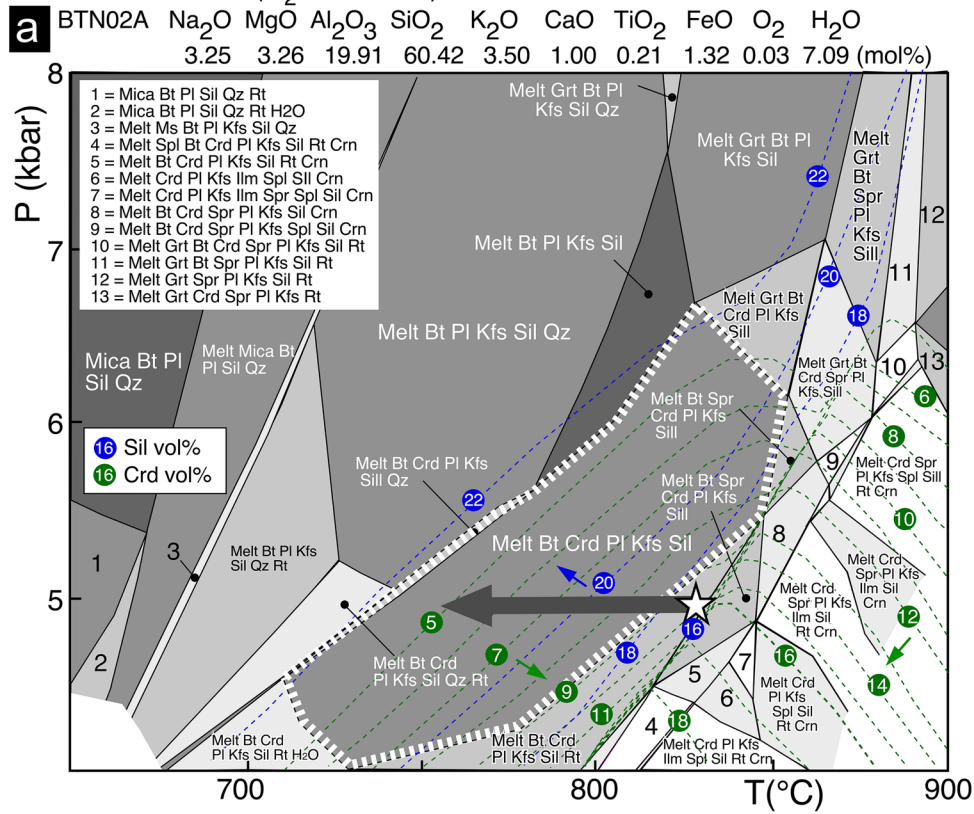
### Tectonic significance

In East Antarctica, a counter-clockwise  $P$ – $T$  path and IBC have been reported from basement rocks of the Rayner Complex (Fig. 1a) in McRobertson Land and the Northern Prince Charles Mountains (Fig. 1a; Boger and White 2003; Halpin et al. 2007; Morrissey et al. 2015). This metamorphism is thought to have been related to the emplacement of voluminous charnockite rocks at 990–900 Ma. In East Antarctica, a counter-clockwise  $P$ – $T$  path with IBC has also been proposed for the SW terrane of the Sør Rondane Mountains in Eastern Dronning Maud Land (Baba et al. 2013). The SW terrane reached granulite-facies conditions of up to  $\sim$ 9 kbar and  $\sim$ 900 °C (Baba et al. 2013) as a result of tectonic loading

from over-thrusting of the NE terrane (Osanai et al. 2013). The timing of peak metamorphism has been constrained at 650–600 Ma (Osanai et al. 2013). Recently, a counter-clockwise  $P$ – $T$  path at 620–530 Ma (Kitano et al. 2023) was also proposed for Tenmondai Rock in the LHC (Fig. 1b) based on the textural relation of which the inclusion phase, spinel and ilmenite within sillimanite and kyanite, and kyanite and rutile in the matrix (Baba et al. 2023). However, the tectonic process that caused such metamorphism remains unclear.

The Botnnuten gneisses did not reach high- $P$  ( $\sim$ 6 kbar), and the geothermal gradient is assumed to be  $>$ 40 °C/km ( $>$ 1400 °C/GPa). This value is relatively high compared to other instance of granulite–UHT metamorphism at 600–500 Ma (Brown 2007; Brown and Johnson 2019). The high geothermal gradient at Botnnuten is obtained at the peak metamorphism, which is not associated with the ITD and is an unusual result in the continent-continent collisional setting of the LHC. Kelsey and Hand (2015) reviewed tectonic settings to achieve the condition of the high- $T$  to UHT granulite facies conditions. They summarized that granulites with near-IBC along counter-clockwise  $P$ – $T$  paths have historically been interpreted to develop in regions that include synchronous magmatism that either underplates or ‘overacretes’ (Wells 1980; Bohlen 1991; Kelsey and Hand 2015 references therein). In the case of the granulite characterized by a near IBC  $P$ – $T$  path, it is considered to have formed by lithospheric extension tectonics and is deemed to occur at the base of regular thickness crust (Sandiford and Powell 1986; Harley 1989). They also associated with long crustal residence times and low erosion rates (Sandiford and Powell 1986; Kelsey and Hand 2015 further reference therein). The 2D petrological–thermomechanical numerical models by Sizova et al. (2014) predicted that metamorphic rocks recording counter-clockwise metamorphic  $P$ – $T$  paths followed by IBC could be formed by assuming a hot collision regime, involving shortening and thickening of hot lithosphere (Figs. 3f and 7c in Sizova et al. 2014). Recently, Jiao et al. (2023) summarized the tectonic settings that generate UHT (high- $T$  granulite) metamorphism and divided it into 1) an arc–back-arc system involving a thinned lithosphere or orogenic plateaus and 2) an orogenic plateau accompanied by radiogenic heating during thickening. According to their calculated  $P$ – $T$  paths using numerical modeling for various tectonic settings, the lithospheric peeling model involving mantle upwelling is applicable to the low- $P$  and IBC paths inferred in this study (Fig. 5a and h in Jiao et al. 2023). To achieve low- $P$  and high- $T$  conditions at Botnnuten, the rocks, therefore, likely experienced additional heat flux from the mantle or heat advection due to magmatism at mid-crustal levels, which may cause by crustal extension or crustal peeling (Jiao et al. 2023). In addition, the IBC path recorded

Model Crd-domain ( $H_2O=1.0$  LOI)



Model Crd-domain ( $H_2O=0.5$  LOI)

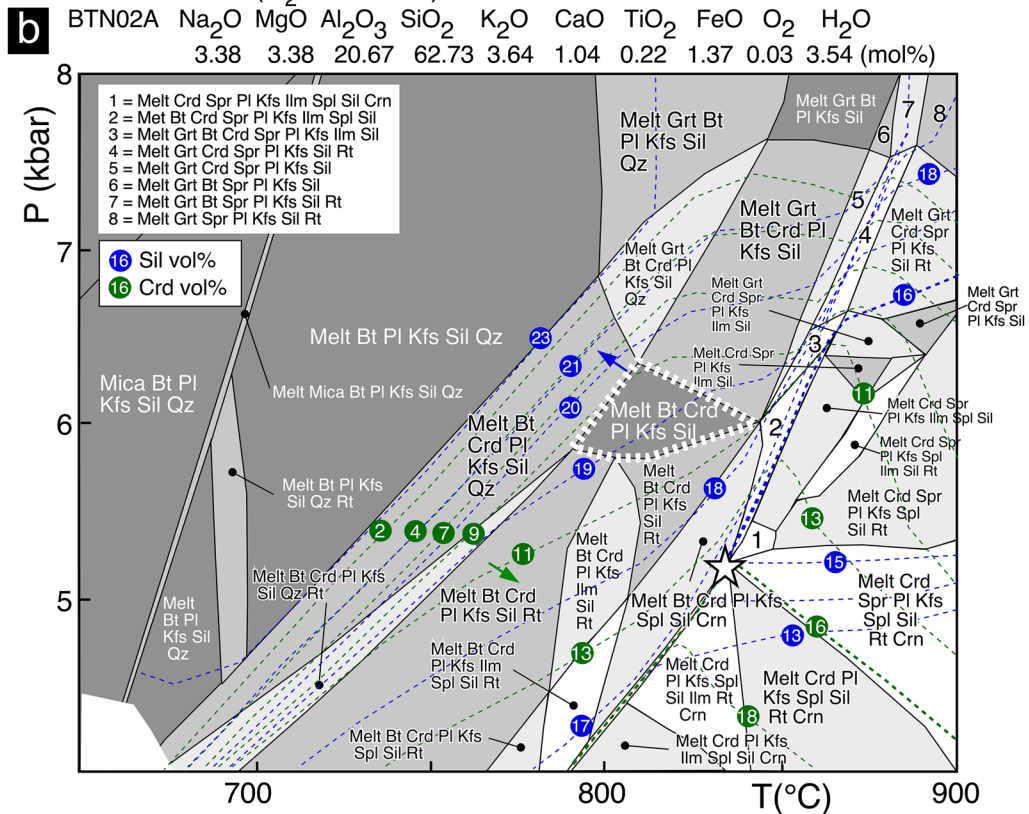




**Fig. 10** NCKFMASHTO  $P$ – $T$  pseudosection using the large-cordierite domain composition of BTN02A (Model Crd-domain). **a** Result of the Crd-domain assuming  $H_2O=1.0$  LOI. **b** Result of the Crd-domain assuming  $H_2O=0.5$  LOI. Modal abundance isopleths are shown for sillimanite and cordierite. The white dashed area represents a stable field of the mineral assemblage of melt-biotite-cordierite-plagioclase-K-feldspar-sillimanite. Small arrows represent an increased trend of modal abundance of sillimanite and cordierite. A star marks the  $P$ – $T$  condition estimated from modal abundance isopleths of cordierite and sillimanite. The arrow in **a** indicates the inferred  $P$ – $T$  path based on the increase and decrease trend of a modal abundance of cordierite and sillimanite

by rocks at Botnnuten implies that they cooled over a long duration at mid-crustal levels due to minimal exhumation of over-thickened crust. These facts conflict with the concept that Botnnuten is a part of the LHC that is considered to have been metamorphosed in an overall orogenic setting.

The past heat flux and advection from the mantle and magmatism would produce voluminous igneous rock; where is the geological evidence preserved? Given that Botnnuten is an isolated inland nunatak, surrounded by an ice sheet, it is difficult to establish its tectonic relationship to surrounding lithologies. In the LHC, Strandnibba and Inhovde (Fig. 1b) have large exposures near Botnnuten; unfortunately, metamorphic  $P$ – $T$  paths have not been reported in either area. Rocks at Inhovde are hornblende-biotite gneiss, orthopyroxene-bearing orthogneiss (charnockite), garnet-biotite gneiss, mafic granulite, and gneissose granite. The hornblende-biotite gneiss yielded a protolith ages of ca. 981 Ma and a metamorphic age of ca. 574 Ma (Tsunogae et al. 2015). The region from Strandnibba to southern Rundvågshetta is the predominantly orthopyroxene-bearing orthogneiss, yielding protolith ages of 2518–2490 Ma and metamorphic ages of 620–520 Ma (Tsunogae et al. 2014; Dunkley et al. 2020). These regions have similar age relationships with the Botnnuten rocks; thus, Dunkley et al. (2020) regarded Botnnuten a part of the Rundvågshetta Suite (Fig. 1b). However, as mentioned above, the metamorphic conditions differ between the two regions. Overall, no geological evidence suggests voluminous magmatism and additional heat flux from the mantle in nearby exposures to Botnnuten in the LHC during metamorphism at Botnnuten (ca. 590–550 Ma).

The basement rocks of the Yamato Mountains (Fig. 1b) are composed of granulite- to amphibolite-facies metamorphic rocks and voluminous granitoids. The estimated  $P$ – $T$  conditions of granulite-facies metamorphism in the area are < 6 kbar and ~ 750 °C (Asami and Shiraishi 1985). Asami and Shiraishi (1985) reported the development of garnet coronas and quartz between anorthite and wollastonite in calc-silicate gneisses from this region, indicating high-temperature isobaric cooling (e.g., Fitzsimons and Harley 1994; Dasgupta and Pal 2001). The granitoids in the Yamato Mountains, which are mainly syenite, occur as lit-par-lit injection layers within the host gneiss (Asami and

Shiraishi 1985). If these intrusions were the heat source low- $P$ /high- $T$  metamorphism would have been likely. Shiraishi et al. (2003) reported two thermal events for Yamato Mountain— an older event (ca. ~ 620 Ma) thought to be associated with granulite-facies metamorphism and granite magmatism, and a younger event (~ 535 Ma), which involved amphibolite-facies metamorphism and quartz-monzonite magmatism, which followed the widespread intrusion of syenite pluton. The metamorphic age of 590–550 Ma for the Botnnuten rocks (Dunkley et al. 2020) is slightly older than the timing of widespread syenite magmatism. Therefore, a direct tectonic and metamorphic connection between Botnnuten and the Yamato Mountains remains problematic. To further explore the metamorphic  $P$ – $T$  path, geochemical and geochronological studies to clarify the magmatism and tectonic setting of the entire LHC, including unexplored localities, are necessary to understand the geological processes, including crustal thinning by extensional or crustal delamination in a continent-continent collisional setting.

## Conclusions

We investigated the  $P$ – $T$  evolution of a suite of cordierite- and spinel-bearing gneisses from Botnnuten, East Antarctica, using mineral chemistry, petrography, and pseudosection modeling, and determined that the rocks at Botnnuten underwent high- $T$ /low- $P$  metamorphism (~ 5.0–6.2 kbar and ~ 850 ± 20 °C) and IBC towards ~ 800–810 °C. The studied samples are the first cordierite-bearing gneisses to have been identified at Botnnuten, and the first megacrystic cordierite to be observed in the LHC region. Pseudosection models were constructed using 1) whole-rock compositional data (WR), 2) WR incorporating  $O_2$  (WR+O), and 3) a domain composition for the megacrystic cordierite and surrounding minerals. The Botnnuten rocks experienced a high thermal gradient (> 40 °C/km), implying that metamorphism was driven by additional heat flux from the mantle or heating by magmatism. The IBC trajectory suggests that Botnnuten was situated at mid-crustal levels for a long duration, and that the rocks were not rapidly exhumed due to orogenic collapse. This geological process occurred in a part of the orogenic system and was related to the formation of the Gondwana supercontinent. The inferred  $P$ – $T$  path and peak metamorphic conditions at Botnnuten are similar to those reported for the Yamato Mountains, located approximately 150 km to the southwest of the study area. There is a slight age difference between the metamorphism at Botnnuten and magmatism in the Yamato Mountains, requiring further detailed studies into the connection between the two regions.

**Supplementary Information** The online version contains supplementary material available at <https://doi.org/10.1007/s00710-024-00859-0>.

**Acknowledgements** We would like to thank the members of the 58th Japan Antarctic Research Expedition, and the crew of the icebreaker Shirase. This study is a part of the Science Program of Japanese Antarctic Research Expedition (JARE). It was supported by the National Institute of Polar Research (NIPR) under MEXT. This work was partly supported by the NIPR [General Collaboration Projects 25–17 and 2–20], the Research Organization of Information and Systems [ROIS-DS-JOINT 004RP2018], and the Japan Society for the Promotion of Science (JSPS) [17H02976 to T.H. and 18H01313 to A.K.]. We thank anonymous reviewers for constructive comments, and Andreas Möller and Lutz Nasdala for valuable suggestions and careful editorial handling.

**Funding** National Institute of Polar Research [General Collaboration Projects 25–17 and 2–20]. The Research Organization of Information and Systems [ROIS-DS-JOINT 004RP2018]. The Japan Society for the Promotion of Science (JSPS) [17H02976 to T.H. and 18H01313 to A.K.].

**Availability of data and materials** All data presented in the text of the article are fully available without restriction from authors upon request.

## References

- Asami M, Shiraishi K (1985) Retrograde metamorphism in the Yamato Mountains, East Antarctica. *Memoires Natl Inst Polar Res Spec Issue 37*:147–163
- Baba S, Osanai Y, Nakano N, Owada M, Hokada T, Horie K, Adachi T, Toyoshima T (2013) Counterclockwise  $P$ – $T$  path and isobaric cooling of metapelites from Brattnipene, Sør Rondane Mountains, East Antarctica: Implications for a tectonothermal event at the proto-Gondwana margin. *Precambrian Res* 234:210–228
- Baba S, Osanai Y, Adachi T, Nakano N, Hokada T, Toyoshima T (2019) Metamorphic  $P$ – $T$  conditions and variation of REE between two garnet generations from granulites in the Sør-Rondane mountains, East Antarctica. *Mineral Petrol* 113:821–845
- Baba S, Hokada T, Kamei A, Kitano I, Motoyoshi Y, Nantasin P, Setiawan NI, Dashbaatar D (2021) Tectono-metamorphic evolution and significance of shear-zone lithologies in Akebono Rock, Lützow-Holm Complex East Antarctica. *Antarctic Sci* 33:52–72
- Baba S, Horie K, Hokada T, Takehara M, Kamei A, Kitano I, Motoyoshi Y, Nantasin P, Setiawan NI, Dashbaatar D (2022) Newly found Tonian metamorphism in Akebono Rock, eastern Dronning Maud Land, East Antarctica. *Gondwana Res* 105:243–261
- Baba S, Nantasin P, Kamei A, Kitano I, Motoyoshi Y, Setiawan NI, Dashbaatar D, Hokada T (2023) Counter-clockwise  $P$ – $T$  history deduced from kyanite-bearing pelitic gneiss in Tenmondai Rock, Lützow-Holm Complex. *East Antarctica J Mineral Petrol Sci* 118:S001
- Boger SD, White RW (2003) The metamorphic evolution of metapelitic granulites from Radok Lake, northern Prince Charles Mountains, east Antarctica: evidence for an anticlockwise  $P$ – $T$  path. *J Metamorph Geol* 21:285–298
- Boger SD, White RW, Schulte B (2012) The importance of iron speciation ( $\text{Fe}^{+2}/\text{Fe}^{+3}$ ) in determining mineral assemblages: an example from the high-grade aluminous metapelites of southeastern Madagascar. *J Metamorph Geol* 30:997–1018
- Boger SD, Hirdes W, Ferreira CAM, Jenett T, Dallwig R, Fanning CM (2015) The 580–520 Ma Gondwana suture of Madagascar and its continuation into Antarctica and Africa. *Gondwana Res* 28:1048–1060
- Bohlen SR (1987) Pressure-temperature-time paths and a tectonic model for the evolution of granulites. *J Geol* 95:617–632
- Bohlen SR (1991) On the formation of granulites. *J Metamorph Geol* 9:223–229
- Brown M (1993)  $P$ – $T$ – $t$  evolution of orogenic belts and the causes of regional metamorphism. *J Geol Soc London* 150:227–241
- Brown M (2007) Metamorphic conditions in orogenic belts: a record of secular change. *Int Geol Rev* 49:193–234
- Brown M, Johnson T (2019) Time's arrow, time's cycle: Granulite metamorphism and geodynamics. *Mineral Mag* 83:323–338
- Clarke GL, Powell R, Guiraud M (1989) Low-pressure granulite facies metapelitic assemblages and corona textures from MacRobertson land, east Antarctica: the importance of  $\text{Fe}_2\text{O}_3$  and  $\text{TiO}_2$  in accounting for spinel-bearing assemblages. *J Metamorph Geol* 7:323–335
- Connolly JAD (2005) Computation of phase equilibria by linear programming: a tool for geodynamic modeling and its application to subduction zone decarbonation. *Earth Planet Sci Lett* 236:524–541
- Dasgupta S, Pal S (2001) Origin of grandite garnet in calc-silicate granulites: mineral–fluid equilibria and petrogenetic grids. *J Petrol* 46:1045–1076
- Deer WA, Howie RA, Zussman J (1992) An introduction to the rock forming minerals, 2nd edn. Longman Scientific and Technical, New York, Essex, p 696
- Dunkley D, Hokada T, Shiraishi K, Hiroi Y, Nogi Y, Motoyoshi Y (2020) Geological subdivision of the Lützow-Holm Complex in East Antarctica: From the Neoproterozoic to the Neoproterozoic. *Polar Sci* 26:100606
- Dunkley DJ, Shiraishi K, Motoyoshi Y, Tsunogae T, Miyamoto T, Hiroi Y, Carson CJ (2014) Deconstructing the Lützow-Holm Complex with zircon geochronology. *Abstr of 7th Int SHRIMP workshop program*, pp 116–121
- Durgalakshmi SK, Williams IS, Reddy DH, Satishi-Kumar M, Jones N, Malaviarachchi SPK, Samuel VO, George PM (2021) The timing, duration and conditions of UTH metamorphism in remnants of the former eastern Gondwana. *J Petrol* 62:1–38
- England PC, Thompson AB (1984) Pressure Temperature time paths of regional metamorphism I. Heat transfer during the evolution of regions of thickened continental crust. *J Petrol* 25:894–928
- Fitzsimons ICW (2000) Grenville-age basement provinces in East Antarctica: evidence for three separate collisional orogens. *Geology* 28:879–882
- Fitzsimons ICW, Harley SL (1994) Garnet coronas in scapolite-wollastonite calc-silicates from East Antarctica: the application and limitations of activity-corrected grids. *J Metamorph Geol* 6:761–777
- Fuhrman ML, Lindsley DH (1988) Ternary-Feldspar Modelling and Thermometry. *Am Mineral* 73:201–215
- Halpin JA, Clarke GL, White RW, Kelsey DE (2007) Contrasting  $P$ – $T$  paths for Neoproterozoic metamorphism in MacRobertson and Kemp Lands, East Antarctica. *J Metamorph Geol* 25:683–701
- Harley SL (1989) The origins of granulites: a metamorphic perspective. *Geol Mag* 126:215–247
- Hiroi Y, Shiraishi K, Motoyoshi Y (1991) Late Proterozoic paired metamorphic complexes in East Antarctica, with special reference to the tectonic significance of ultramafic rocks. In: Thomson MRA, Crame JA, Thomson JW (eds) *Geological Evolution of Antarctica*. Cambridge University Press, Cambridge, pp 83–87
- Hiroi Y, Hokada T, Kato M, Yanagi A, Adachi T, Osanai Y, Motoyoshi Y, Shiraishi K (2019) Felsite–nanogranite inclusions and three  $\text{Al}_2\text{SiO}_5$  polymorphs in the same garnet in ultrahigh-temperature granulites from Rundvågshetta, Lützow-Holm Complex, East Antarctica. *J Mineral Petrol Sci* 114:60–78
- Holland TJB, Powell R (2011) An improved and extended internally consistent thermodynamic dataset for phases of petrological interest, involving a new equation of state for solids. *J Metamorph Geol* 29:333–383

- Holland TJB, Green ECR, Powell R (2018) Melting of Peridotites through to Granites: A Simple Thermodynamic Model in the System KNCFMASH+H<sub>2</sub>O. *J Petrol* 59:881–900
- Ishikawa M, Motoyoshi Y, Fraser GL, Kawasaki T (1994) Structural evolution of Rundvågshetta region, Lützow-Holm bay, East Antarctica. *Proc NIPR Symp Antarctic Geosci* 7:69–89
- Iwamura S, Tsunogae T, Kato M, Koizumi T, Dunkley D (2013) Petrology and phase equilibrium modeling of spinel-sapphirine-bearing mafic granulite from Akarui Point, Lützow-Holm Complex, East Antarctica: Implications for the  $P$ – $T$  path. *J Mineral Petrol Sci* 108:345–350
- Jacobs J, Thomas RJ (2004) Himalayan-type indenter-escape tectonics model for the southern part of the late Neoproterozoic-early Paleozoic East African-Antarctic orogeny. *Geology* 32:721–724
- Jacobs J, Elburg M, Läufer A, Kleinhanns IC, Henjes-Kunst F, Estrada S, Ruppel A, Damaske D, Montero P, Bea F (2015) Two distinct Late Mesoproterozoic/Early Neoproterozoic basement provinces in central/eastern Dronning Maud Land, East Antarctica: the missing link, 15–21°E. *Precambrian Res* 265:249–272
- Jiao S, Brown M, Mitchell RN, Chowdhury P, Clark C, Chen L, Chen Y, Korhonen F, Huang G, Guo J (2023) Mechanism to generate ultrahigh-temperature metamorphism. *Nature Rev Earth and Environ* 4:298–318
- Kawakami T, Hokada T, Sakata S, Hirata T (2016) Possible polymetamorphism and brine infiltration recorded in the garnet-sillimanite gneiss, Skallevikshalsen, Lützow-Holm Complex, East Antarctica. *J Mineral Petrol Sci* 111:129–143
- Kawasaki T, Nakano N, Osanai Y (2011) Osumilite and a spinel+quartz association in garnet-sillimanite gneiss from Rundvågshetta, Lützow-Holm Complex, East Antarctica. *Gondwana Res* 19:430–445
- Kelsey DE, Hand M (2015) On ultrahigh temperature crustal metamorphism: Phase equilibria, trace element thermometry, bulk composition, heat sources, timescales and tectonic settings. *Geosci Front* 6:311–356
- Kimura J, Yamada Y (1996) Evaluation of major and trace element XRF analyses using a flux to sample ratio of two to one glass beads. *J Mineral Petrol Econ Geol* 91:62–72
- Kitano I, Hokada T, Baba S, Kamei A, Motoyoshi Y, Nantasin P, Setiawan NI, Dashbaatar D, Toyoshima T, Ishikawa M, Katori T, Nakano N, Osanai Y (2023) Zircon geochronology of high-grade metamorphic rocks from outcrops along the Prince Olav Coast, East Antarctica: Implications for multi-thermal events and regional correlations. *J Mineral Petrol Sci* 118:S009
- Meert J (2003) A synopsis of events related to the assembly of eastern Gondwana. *Tectonophysics* 362:1–40
- Morrissey L, Hand M, Kelsey DE (2015) Multi-stage metamorphism in the Rayner-Eastern Ghats Terrane:  $P$ – $T$ – $t$  constraints from the northern Prince Charles Mountains, east Antarctica. *Precambrian Res* 267:137–169
- Motoyoshi Y, Ishikawa M (1997) Metamorphic and structural evolution on granulites from Rundvågshetta, Lützow-Holm Bay, East Antarctica. In: Ricci CA (ed) *The Antarctic Region: Geological Evolution and Processes*. Terra Antarctica Publication, Siena, Italy, pp 65–72
- Motoyoshi Y, Shiraishi K (1985) Petrography and geothermometry-geobarometry of Botnnuten, East Antarctica. *Memoires Natl Inst Polar Res Spec Issue* 37:127–146
- Osanai Y, Nogi Y, Baba S, Nakano N, Adachi T, Hokada T, Toyoshima T, Owada M, Satish-Kumar M, Kamei A, Kitano I (2013) Geologic evolution of the Sør Rondane Mountains, East Antarctica: collision tectonics proposed based on metamorphic processes and magnetic anomalies. *Precambrian Res* 234:8–29
- Osanai Y, Sajeev K, Nakano N, Kitano I, Kehelpannala WKV, Kato R, Adachi T, Malaviarachchi SPK (2016) UHT granulites of the Highland Complex, Sri Lanka II: Geochronological constraints and implications for Gondwana correlation. *J Mineral Petrol Sci* 111:157–169
- Palin RM, Weller OM, Waters DJ, Dyck B (2016) Quantifying geological uncertainty in metamorphic phase equilibria modelling: a Monte Carlo assessment and implications for tectonic interpretations. *Geosci Front* 7:591–607
- Ruppel A, Jacobs J, Eagles G, Läufer A, Jokat W (2018) New geophysical data from a key region in East Antarctica: estimates for the spatial extent of the Tonian Oceanic Arc Super Terrane (TOAST). *Gondwana Res* 59:97–107
- Sandiford M, Powell R (1986) Deep crustal metamorphism during continental extension: modern and ancient examples. *Earth Planet Sci Lett* 79:151–158
- Santoshi M, Yoshida M (1992) A petrologic and fluid inclusion study of charnockites from the Liützow-Holm Bay region, East Antarctica: Evidence for fluid-rich metamorphism in the lower crust. *Lithos* 29:107–126
- Shiraishi K, Ellis DJ, Hiroi Y, Fanning CM, Motoyoshi Y, Nakai Y (1994) Cambrian orogenic belt in east Antarctica and Sri Lanka: implications for Gondwana assembly. *J Geol* 102:47–65
- Shiraishi K, Ellis DJ, Fanning CM, Hiroi Y, Kagami H, Motoyoshi Y (1997) Reexamination of the metamorphic and protolith ages of the Rayner complex, Antarctica: Evidence for the Cambrian (Pan-African) regional metamorphic event. In: Ricci CA (ed) *The Antarctic Region: Geological Evolution and Processes*. Terra Antarctica Publication, Siena, Italy, pp 79–88
- Shiraishi K, Hokada T, Fanning CM, Misawa K, Motoyoshi Y (2003) Timing of thermal events in eastern Dronning Maud Land, East Antarctica. *Polar Geosci* 16:76–99
- Shiraishi K, Dunkley DJ, Hokada T, Fanning CM, Kagami H, Hamamoto T (2008) Geochronological constraints on the Late Proterozoic to Cambrian crustal evolution of eastern Dronning Maud Land, East Antarctica: a synthesis of SHRIMP U-Pb age and Nd model age data. *Geol Soc London Spec Publ* 308:21–67
- Shiraishi K, Hiroi Y, Motoyoshi Y (1989) Antarctic Geological Map Series, Sheet 12 Prince Olav Coast. NIPR, Tokyo
- Sizova E, Gerya T, Brown M (2014) Contrasting styles of Phanerozoic and Precambrian continental collision. *Gondwana Res* 25:522–545
- Stephenson NCN (1977) Coexisting hornblendes and biotites from Precambrian gneiss of the south coast of Western Australia. *Lithos* 10:9–27
- Stern RJ (1994) Arc assembly and continental collision in the Neoproterozoic East African Orogen: implications for consolidation of Gondwanaland. *Annu Rev Earth Planet Sci* 22:319–351
- Suzuki K, Kawakami T (2019) Metamorphic pressure-temperature conditions of the Lützow-Holm Complex of East Antarctica deduced from Zr-in-rutile geothermometer and Al<sub>2</sub>SiO<sub>5</sub> minerals enclosed in garnet. *J Mineral Petrol Sci* 114:267–279
- Takahashi K, Tsunogae T (2017) Carbonic fluid inclusions in a garnet-pyroxene granulite from Austhovde in the Lützow-Holm Complex, East Antarctica: Implications for a decompressional  $P$ – $T$  path. *J Mineral Petrol Sci* 112:132–137
- Takahashi K, Tsunogae T, Santoshi M, Takamura Y (2018) Paleoproterozoic (ca. 1.8 Ga) arc magmatism in the Lützow-Holm Complex, East Antarctica: Implications for crustal growth and terrane assembly in erstwhile Gondwana fragments. *J Asian Earth Sci* 157:245–265
- Takamura Y, Tsunogae T, Santosh M, Tsutsumi Y (2018) Detrital zircon geochronology of the Lützow-Holm Complex, East Antarctica: Implications for Antarctica-Sri Lanka correlation. *Geosci Front* 9:355–375
- Takamura Y, Tsunogae T, Tsutsumi Y (2020) U-Pb geochronology and REE geochemistry of zircons in mafic granulites from the Lützow-Holm complex, East Antarctica: Implications for the timing and  $P$ – $T$  path of post-peak exhumation and Antarctica-Sri Lanka correlation. *Precambrian Res* 348:105850

- Thompson AB, England PC (1984) Pressure Temperature time paths of regional metamorphism II. Their inference and interpretation using mineral assemblage in metamorphic rocks. *J Petrol* 25:929–955
- Tsunogae T, Dunkley DJ, Horie K, Endo T, Miyamoto T, Kato M (2014) Petrology and SHRIMP zircon geochronology of granulites from Vesleknausen, Lützow-Holm Complex, East Antarctica: Neoproterozoic magmatism and Neoproterozoic high-grade metamorphism. *Geosci Front* 5:167–182
- Tsunogae T, Yang QY, Santosh M (2015) Early Neoproterozoic arc magmatism in the Lützow-Holm Complex, East Antarctica: Petrology, geochemistry, zircon U–Pb geochronology and Lu–Hf isotopes and tectonic implications. *Precambrian Res* 266:467–489
- Wells PRA (1980) Thermal models for the magmatic accretion and subsequent metamorphism of continental crust. *Earth Planet Sci Lett* 46:253–265
- Wen S, Nekvasil H (1994) Solvcalc: an interactive graphics program package for calculating the ternary feldspar solvus and for two-feldspar geothermometry. *Comput Geosci* 20:1025–1040
- Wheller CJ, Powell R (2014) A new thermodynamic model for sapphirine: calculated phase equilibria in  $K_2O$ – $FeO$ – $MgO$ – $Al_2O_3$ – $SiO_2$ – $H_2O$ – $TiO_2$ – $Fe_2O_3$ . *J Metamorph Geol* 32:287–299
- White RW, Powell R, Clarke GL (2002) The interpretation of reaction textures in Fe rich metapelitic granulites of the Musgrave Block, central Australia: constraints from mineral equilibria calculations in the system  $K_2O$ – $FeO$ – $MgO$ – $Al_2O_3$ – $SiO_2$ – $H_2O$ – $TiO_2$ – $Fe_2O_3$ . *J Metamorph Geol* 20:41–55
- White RW, Powell R, Holland TJB, Johnson TE, Green ECR (2014) New mineral activity-composition relations for thermodynamic calculations in metapelitic systems. *J Metamorph Geol* 32:261–286
- Yoshimura Y, Motoyoshi Y, Miyamoto T (2008) Sapphirine+quartz association in garnet: implication for ultrahigh-temperature metamorphism at Rundvågshetta, Lützow-Holm Complex, East Antarctica. *Geol Soc London Spec Publ* 308:377–390

**Publisher's Note** Springer Nature remains neutral with regard to jurisdictional claims in published maps and institutional affiliations.

Springer Nature or its licensor (e.g. a society or other partner) holds exclusive rights to this article under a publishing agreement with the author(s) or other rightsholder(s); author self-archiving of the accepted manuscript version of this article is solely governed by the terms of such publishing agreement and applicable law.